



The relationship between magma and mineralization in Chaobuleng iron polymetallic deposit, Inner Mongolia



Chen Wu^{a,*}, Biren Wang^b, Zhiguang Zhou^a, Guosheng Wang^a, Andrew V. Zuza^c, Changfeng Liu^d, Tian Jiang^e, Wencan Liu^d, Shiwei Ma^f

^a School of Earth Science and Resources, China University of Geosciences (Beijing), Beijing 100083, China

^b Cores and Samples Center of Land and Resources, CGS, Yanjiao 065201, Hebei, China

^c Nevada Bureau of Mines and Geology, University of Nevada, Reno, NV 89557, USA

^d Institute of Geological Survey, China University of Geosciences (Beijing), Beijing 100083, China

^e School of Ocean Sciences, China University of Geosciences (Beijing), Beijing 100083, China

^f Institute of Geology, Chinese Academy of Geological Sciences, Beijing 100037, China.

ARTICLE INFO

Article history:

Received 15 November 2016

Received in revised form 26 January 2017

Accepted 14 February 2017

Available online 20 February 2017

Handling Editor: F. Pirajno

Keywords:

Skarn

Chaobuleng iron polymetallic deposit

Magmatic hydrothermal mineralization

Magma mixing

F-rich fluid

ABSTRACT

The Chaobuleng iron polymetallic deposit, an important ore system in China that is genetically related to the early Cretaceous Chaobuleng pluton, is located in the eastern part of Lizi Shan-Dong Ujimqin Banner metallogenic belt of Inner Mongolia. To understand the relationship of magmatism and mineralization in this iron polymetallic deposit, we have conducted a detailed geologic field study in conjunction with systematic investigation of U–Pb zircon and Re–Os isochron geochronology, mineralogy, petrology, major- and trace-element geochemistry, and synthesis of existing datasets across the Chaobuleng region. We use these observations to identify the origins and petrogenesis of mafic enclaves and the host granitoid, and to place new constraints on the tectonic setting at the time of magmatism. New U–Pb geochronology of magmatic zircons and Re–Os isochron ages of hydrothermal molybdenite from the iron polymetallic deposit allow us to constrain the sources of the hydrothermal components and the relationship between iron polymetallic mineralization and regional geodynamic evolution. The geology, paragenesis, and estimated *P–T* conditions suggest that the Chaobuleng iron polymetallic deposit was formed as a shallow, proximal skarn deposit. The ore-forming early Cretaceous Chaobuleng pluton can be divided into three distinct units based on crystallization age, texture, and composition: (1) a 138.1–140.6 Ma syenogranite porphyry, (2) a 137.4–138.6 Ma enclave bearing porphyritic syenogranite, and (3) a 133.9–135.98 Ma coarse-grained porphyritic syenogranite. We suggest that the A-type Chaobuleng pluton was formed in a post-orogenic extensional setting with significant magma mixing from high-temperature melts (i.e., a Zr saturation temperature of 800–900 °C). During the magmatic process, the Chaobuleng pluton crystallized under temperatures as low as 720–770 °C and pressures of 0.5–1.0 kbar. The chemical composition of biotite shows that the Chaobuleng magma was enriched in F (1.5–3.5%). We attribute the observed embayed texture of quartz to a three coexisting-phase equilibrium model that operated during the magmatic-hydrothermal transition and can be used to constrain the mineralization process and physico-chemical conditions. Due to a loss of volatiles, the residual melt was quickly quenched and crystallized into a fine-grained groundmass. The Re–Os model ages of samples from the inner pluton–mineralization contact belt are 135.0 ± 2.1 Ma and 131.2 ± 4.1 Ma, and a sample from the outer-contact belt yields an isochron age of 140.7 ± 1.8 Ma. The Chaobuleng deposit formed during protracted activity of the magmatic-hydrothermal system, which is similar to many mineralization systems around the world. However, the major mineralization stage (iron oxide stage) of the Chaobuleng deposit occurred during the early stage of magmatism, consistent with the emplacement time of syenogranite porphyry at ~139 Ma.

© 2017 International Association for Gondwana Research. Published by Elsevier B.V. All rights reserved.

1. Introduction

Iron deposits may be classified as magmatic, sedimentary, and metamorphic (e.g., Dill, 2010; Zhao and Zhou, 2015; Zhang et al., 2014). In China, magmatic iron and metasomatic hydrothermal iron deposits, especially skarn-type iron ores, are the principal sources of high-grade

* Corresponding author.

E-mail address: wuchen2016@cugb.edu.cn (C. Wu).

iron reserves (e.g., Kusky and Li, 2003; Wilde et al., 2002; Zhao et al., 2001; Zhao, 2013; Zhang et al., 2014). The formation of skarn deposits has long been recognized as a dynamic process (Meinert et al., 2005; Dill, 2010). The temporal and spatial evolution of skarn systems reflects the paragenetic sequence of skarn minerals, including pyroxene, garnet, and amphibole, which may provide important information about the formation environment (Meinert et al., 2005).

The tectonic evolution of the Central Asian Orogenic Belt (CAOB) (Fig. 1, inset) (e.g., Sengör et al., 1993; Jahn et al., 2004b; Windley et al., 2007; Xiao et al., 2003, 2009, 2010, 2014; Xiao, 2015; Xiao and Zhao, 2016; Li et al., 2014; Xu et al., 2013; Liu et al., 2015; Wu et al., 2016b) is characterized by bivergent subduction beneath the active southern margin of the Siberia craton and northern margin of the North China craton (Xiao et al. 2003, 2009; Wu et al., 2016b). The eastern Central Asian Orogenic Belt in Inner Mongolia, northeastern China, formed primarily in the Paleozoic due to the southward subduction of the Paleo-Asian Ocean and the accompanying accretion of oceanic plate sediments, oceanic crust, and magmatic arcs (including oceanic island arcs and related forearc and back-arc basins) to the northern margin of the North China craton (Xiao et al., 2003; De Jong et al.,

2006; Windley et al., 2007; Li et al., 2014; Wu et al., 2016b). Establishing the processes and controls for the generation of the widely distributed Paleozoic-Mesozoic magmatic belt in eastern China remains a major challenge in interpreting the tectonic evolution of the CAOB.

The Great Xing'an Range (also referred to as the Great Hinggan Range in the literature) is an important metallogenic province in northern China that hosts a variety of ore systems (e.g., Chen et al., 2011; Li et al., 2012; Zhai et al., 2013, 2014; Wu et al., 2014, 2015, 2016a). More than 10 large- and medium-sized Cu–Fe–Sn–Ag deposits (e.g., Zhai et al., 2013, Wu et al., 2014, 2015) have been discovered in this district. The Great Xing'an Range hosts a number of skarn, porphyry, and epithermal ore deposits, which are all believed to be related to Mesozoic magmatism (Chen et al., 2007; Mao et al., 2003, 2005; Zhai et al., 2013, 2014; Zhao and Zhang, 1997; Wu et al., 2014, 2015, 2016a). Mesozoic igneous rocks are widely distributed across this region, which has been referred to as the Great Xing'an Range Mesozoic Igneous Province (Sengör and Natal'in, 1996). The central segment of the Great Xing'an Range has become a particularly important Cu–Mo metallogenic belt in northern China in recent years (Wu et al., 2014; Wu et al., 2016a)

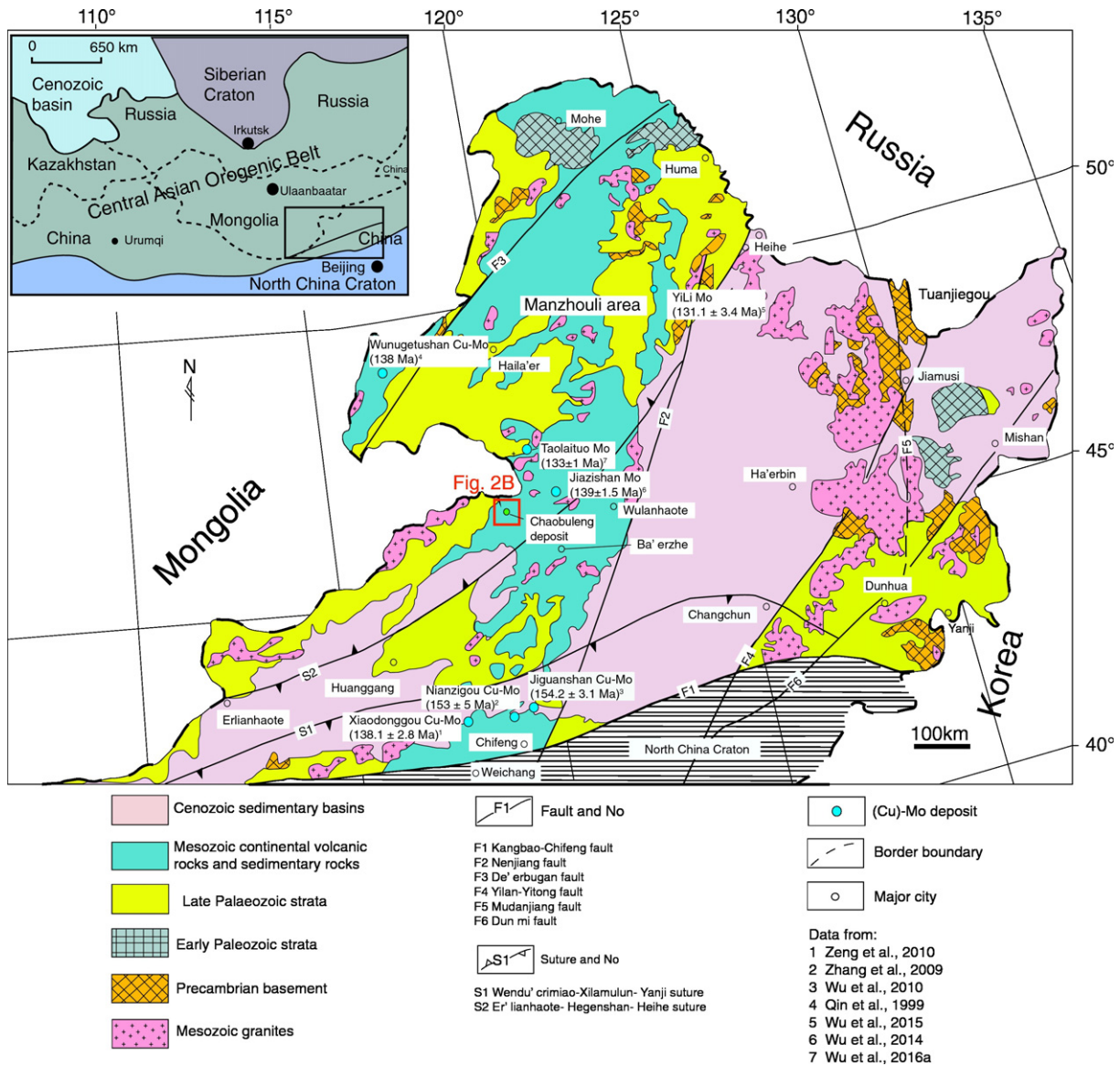


Fig. 1. Regional geologic map of the Great Xing'an Range and adjacent areas in northeast China, modified after Zhou et al. (2012). The blue circles show the main porphyry (Cu)-Mo deposits distributed throughout the Great Xing'an Range. The red box shows the study area in Fig. 2B. (For interpretation of the references to color in this figure legend, the reader is referred to the web version of this article.)

because of the numerous Fe–Cu–Sn–Mo deposits found here. Many of these deposits are epigenetic hydrothermal deposits that are genetically related to Mesozoic magmatism, together with skarn-, vein- and porphyry-type deposits (e.g., Zhai et al., 2014; Wu et al., 2014, 2016a).

In this study, we examine the Chaobuleng deposit, located in the Dong Uqi–Lizi Shan Cu–Mo–Fe (Au) metallogenic belt in the central segment of the Great Xing'an Range (Fig. 2A), and its association with widespread Jurassic–Cretaceous (Yanshanian) plutons (Zhou et al., 2006; Nie et al., 2007; Wang et al., 2014). Direct and accurate dating of magmatic hydrothermal deposits is critical for properly evaluating their relationship to tectonic and magmatic events. We present a detailed investigation of the mineralogy, petrology, and major- and trace-element geochemistry from the Chaobuleng pluton and mafic enclaves. We use these observations to identify the origins and petrogenesis of the mafic enclaves and host granitoid, and to place new constraints on the geodynamic setting and regional tectonic regime at the time of magmatism. We also provide new U–Pb geochronology of magmatic zircons and Re–Os isochron ages of hydrothermal molybdenite from the Chaobuleng Fe polymetallic deposit to constrain the sources of the hydrothermal components and the relationships between iron polymetallic mineralization and regional tectonic setting.

2. Geological setting

2.1. Regional geology

The CAOB formed during the closure of the Paleo-Asian Ocean, and the subsequent convergence between the Siberia and North China cratons (e.g., Sengör et al., 1993; Sengör and Natal'in, 1996; Windley et al., 2007; Kröner et al., 2008, 2010, 2013, 2014; Santosh et al., 2006, 2007; Santosh, 2010; Xiao et al., 2003, 2009, 2010, 2014; Xiao, 2015; Xiao and Zhao, 2016). The CAOB may have been Earth's largest site of juvenile crust formation in the Phanerozoic era (Jahn et al., 2004a; Shi et al., 2010; cf. Kröner et al., 2014). The large orogen is one of the most important regions for Cu, Fe, Sn, Ag, Au and rare metal (Li, Be, Nb, Ta, REE) mineralization in the world (e.g., Mao et al., 2014; Zhai et al., 2014; Wu et al., 2014, 2015, 2016a). The Great Xing'an Range is located near the southeastern boundary of the CAOB, between the Siberian and North China cratons, in western Inner Mongolia (Jahn et al., 2000; Jahn et al., 2004a; Li, 2006; Wu et al., 2012) (Fig. 1). Based primarily on field geological observations and geochronological data, Xu et al. (2013) suggested that the tectonic framework of the CAOB in West Inner Mongolia is characterized by an accretion of different blocks and orogenic belts.

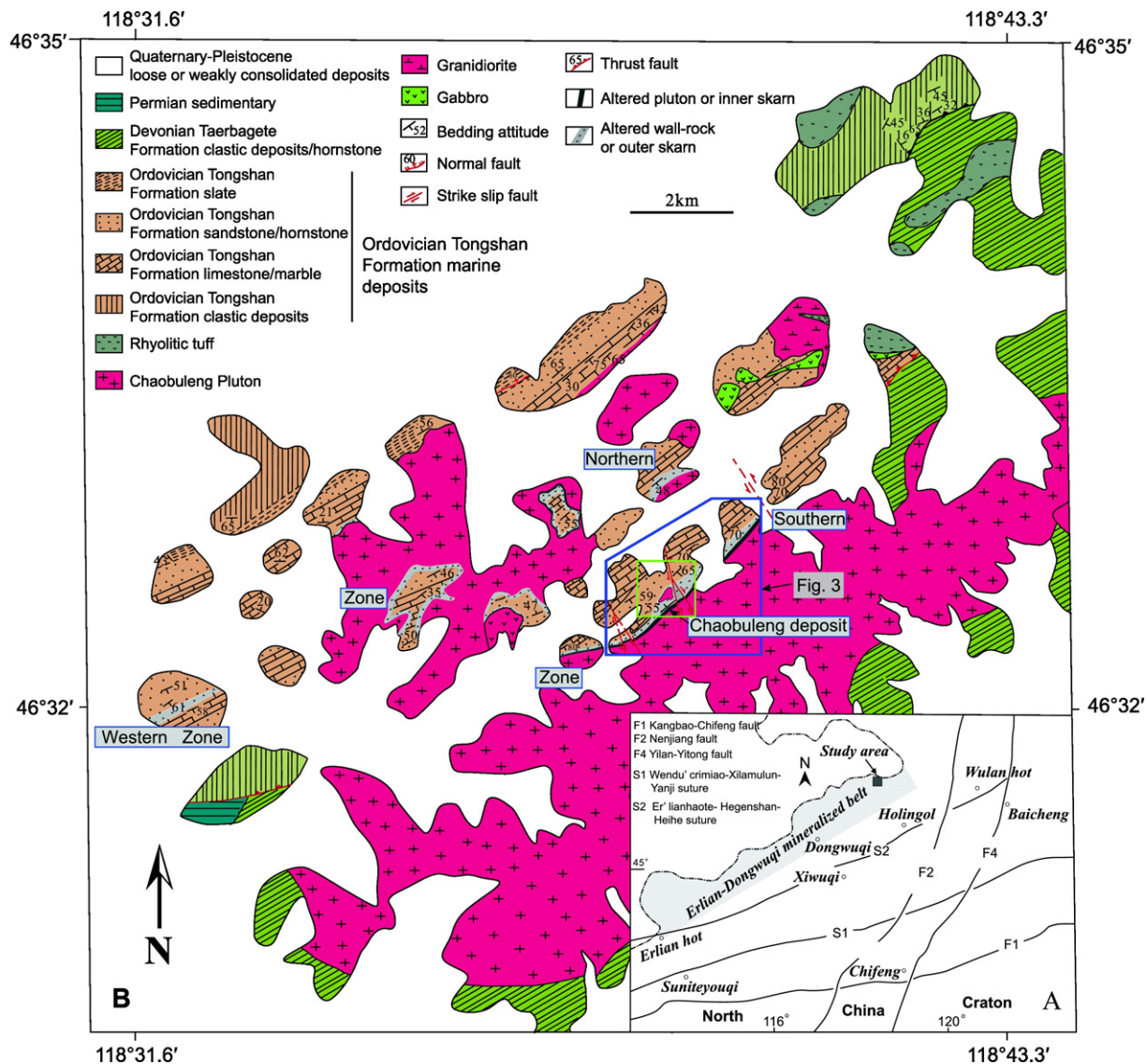


Fig. 2. (A) Generalized geologic map of southern Great Xing'an Range and (B) simplified geological map of the Chaobuleng iron polymetallic deposit in Inner Mongolia, modified from Wang et al., 2014 and based on our own observations. The black box shows the detail geological observations of the southern zone in Fig. 3.

The Great Xing'an Range in northern China is well known for its variety of ore systems. It hosts numerous world-class W–Sn, porphyry Cu–Mo, epithermal Au–Ag, skarn Fe–(Cu), and vein-type Pb–Zn–Ag deposits (e.g., Chen et al., 2011; Li et al., 2012; Zhai et al., 2013, 2014; Mao et al., 2014; Wu et al., 2014, 2015, 2016a) (Fig. 1). These deposits are associated with widespread Yanshanian plutons (Zhou et al., 2006; Nie et al., 2007; Wang et al., 2014). An early episode of magmatism was related to the oblique subduction and breakup of the paleo-Pacific plate. Later magmatism was produced by subduction of the paleo-Pacific plate parallel to the coastline (Hu and Zhou, 2012; Mao et al., 2013). The earlier event was associated with porphyry Cu–Mo deposits and granite-related W–Sn deposits (Mao et al., 2013), where the later late event involved subvolcanic related porphyry Cu–Mo, skarn Fe, and granite-related Sn deposits (Fig. 1). North-south contractional deformation, caused by the convergence of the Siberia and North China cratons, affected most of this region prior to the Early Jurassic. Following the Middle- to Late Jurassic time, the Great Xing'an Range was mostly affected by oblique northwest subduction of the Pacific Ocean plate along the eastern margin of the Eurasian continent (Liu et al., 2014). New Sr–Nd–Pb isotope mapping from this area suggest that Mesozoic crustal growth mainly occurred around the collisional sutures and along the major lithosphere-scale faults (Guo et al., 2010). Early Cretaceous regional deformation was dominated by extension and associated volcanic eruptions (Zhao et al., 2004). Late Mesozoic magmatism was widespread across the Great Xing'an Range (Fig. 1), including multi-phase plutonic and volcanic activity, which shows a close temporal-

spatial relationship with mineralization. The Mesozoic era was the most important period for magmatism and mineralization in northern China, with numerous granitoids associated with Cu, Mo, Fe, Sn, Pb–Zn, and Ag mineralization (e.g. Zhang et al., 2009; Zhai et al., 2014; Wu et al., 2014, 2015, 2016a).

The exposed rocks near the Chaobuleng deposit include the Ordovician Tongshan Formation, middle Devonian Taerbagete Formation, and upper Devonian Angeeryinwula Formation. The Ordovician Tongshan Formation is composed of echinodermmeta fossil-bearing crystalline limestones, low-grade metamorphosed clastic rocks locally interbedded with carbonate rocks which were deposited in a shallow marine environment as a flyschoid formation, and sericite slate (Fig. 2). There is an angular unconformity contact between the Middle Devonian and overlying Permian strata. Permian rocks contain fossils of *Cathaysia* flora (Zhou et al., 2010). The Jurassic Munitu Formation and Baiyingaolao Formation are widely exposed and are composed of an intermediate-felsic volcanic rocks. Red sandy mudstones of the Pliocene Baogedawula Formation are also scattered in the study area. Paleozoic north-northeast-striking faults are exposed throughout the ore district and place Ordovician rocks against Late Devonian strata (Fig. 3A).

Numerous early Paleozoic–Mesozoic plutons are exposed throughout the Chaobuleng region (Wang, et al., 2014), including (1) late Ordovician gabbro (451–452 Ma) and granodiorite (445–448 Ma), (2) Carboniferous coarse-grained syenogranite (325.0–326.6 Ma) and granite (298–311 Ma), (3) late Jurassic (159–161 Ma) granite, and (4) early Cretaceous (130–145 Ma) Chaobuleng ore-related granitoid. Most of the

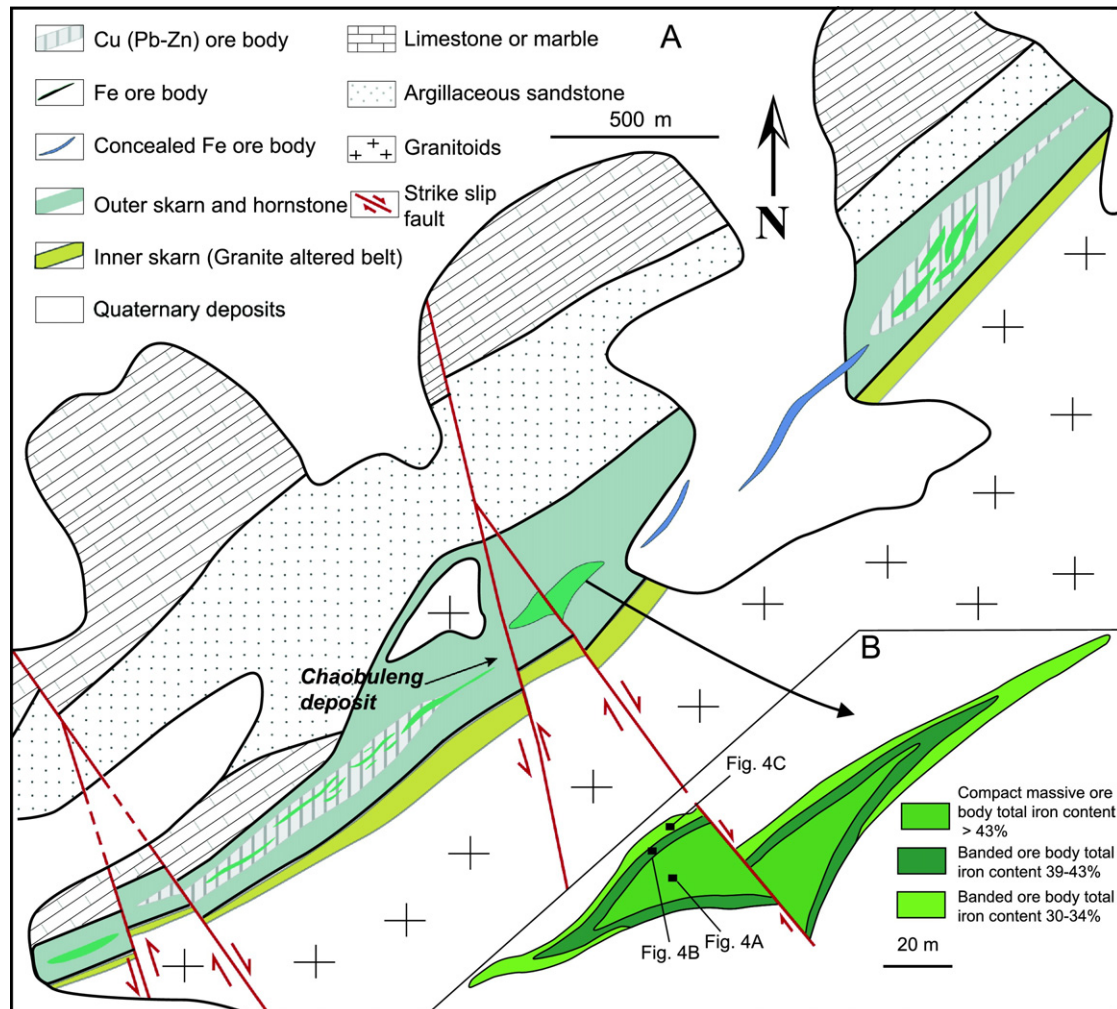


Fig. 3. (A) Detailed geologic map showing the primary mineralization-alteration characteristics of the south zone and (B) structural zoning of oxidized orebodies in Chaobuleng iron polymetallic deposit.

ore bodies in the Chaobuleng mining district are distributed along the margin of the early Cretaceous Chaobuleng pluton.

2.2. Local geology

2.2.1. Geology of ore-related intrusions

The Chaobuleng pluton intrudes marbles and limestones of the Early Ordovician Tongshan Formation and siliciclastic rocks of the Devonian Taerbagete Formation. The pluton, exposed over an area of ca. 84 km² (Fig. 2B), can be divided into three units based primarily on textures and compositions: (1) a syenogranite porphyry, (2) an enclave bearing porphyritic syenogranite, and (3) a coarse-grained porphyritic syenogranite. The syenogranite porphyry unit, located along the northern and southern margins of the Chaobuleng pluton, is exposed over an area of ca. 30 km² (Fig. 2B). This unit intrudes into the Early Ordovician and Devonian formations. Thermal-contact alteration and mineralization of

the outer contact belt are well developed. There is a facies transition between the syenogranite porphyry unit and the coarse-grained porphyritic syenogranite unit. Phenocrysts consist of <10% quartz and feldspar in both the syenogranite porphyry and coarse-grained porphyritic syenogranite samples (Fig. 8B, C). Joints and miarolitic cavities are observed within this syenogranite-porphyry unit. The enclave bearing porphyritic syenogranite is located in the Chaobuleng mining area along the western coast of Weishui Lake and is exposed over ca. 4 km². This unit intrudes into the Early Ordovician Tongshan Formation slate. The composition of the enclaves gradually changes from mafic to more felsic going from the unit's center to its margins. The shape of these enclaves shows plastic-flow characteristics, varying in morphology from rounded to lenticular and elongate. The coarse-grained porphyritic syenogranite, exposed over an area of ca. 50 km², is located in the central of the Chaobuleng pluton. This unit is characterized by more phenocrysts and the existence of lattice jointing (Fig. 8B) (Wang et al., 2014).

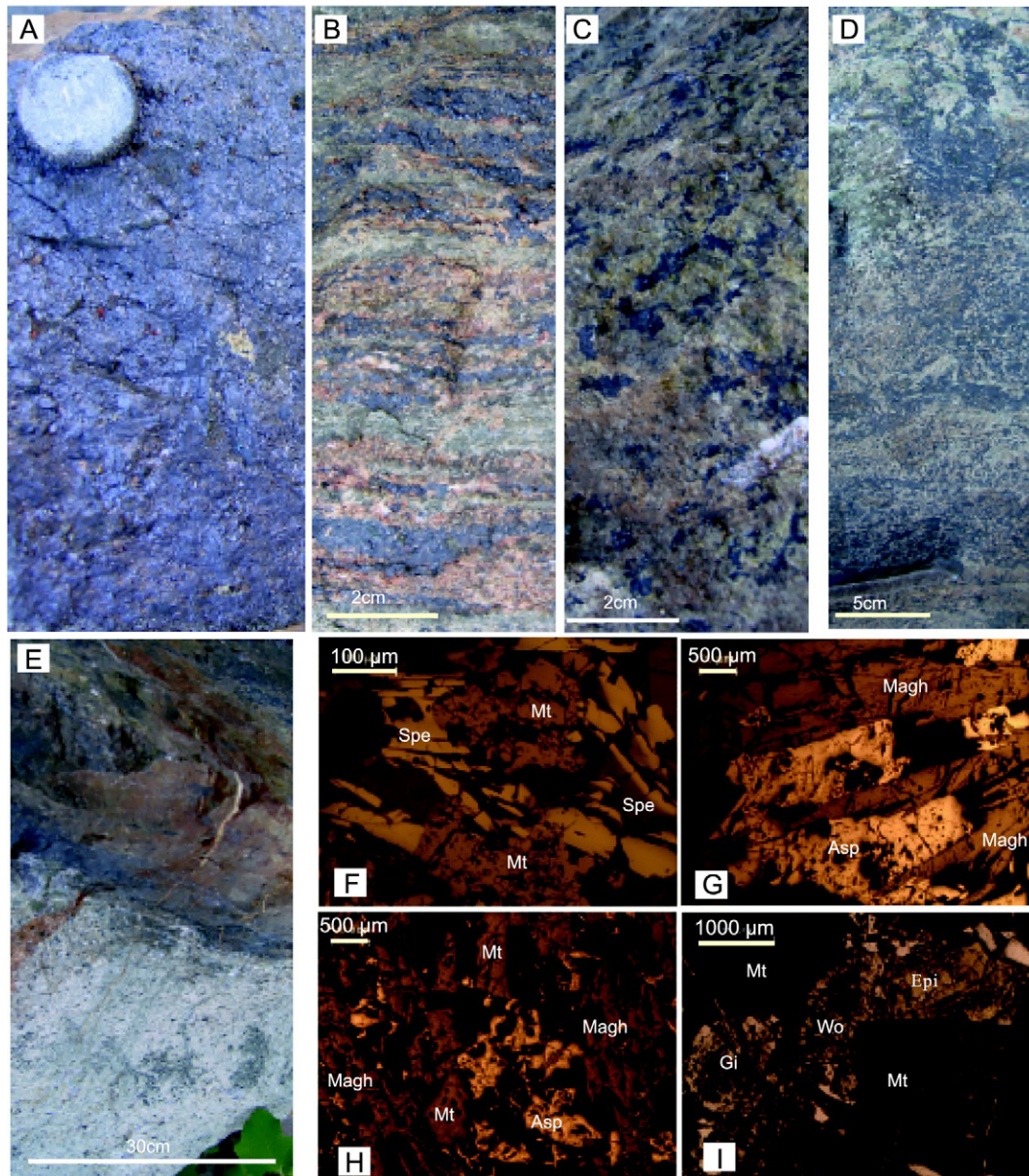


Fig. 4. Photographs showing the textural characteristics of iron oxide ore from the Chaobuleng iron polymetallic deposit. (A–C) Textural zoning in iron oxide ore in Fig. 3B: (A) massive ore in the interior; (B) banded ore in the middle part; (C) disseminated ore at the edge; (D) brecciated skarn with iron oxide cement; and (E) contact between granite with minor disseminated iron oxide and massive ore. (F–I) Photomicrographs of mineral assemblage in iron oxide ore: (F) equilibrium boundary between magnetite and specularite, (G) needle-like maghemite with minor arsenopyrite, (H) assemblage of magnetite, maghemite and minor arsenopyrite, (I) replacement of garnet by an assemblage of magnetite and minor episode. Mt-magnetite; Asp-arsenopyrite; Magh-maghemite; Gr-garnet; Spe-specularite; Epi-episode; Wo-wollastonite.

2.2.2. Geology of the Chaobuleng deposit

The Chaobuleng iron polymetallic deposit is located to the north of the Wendu'crimiao-Xilamulun-Yanji suture (Xiao et al., 2003) in the Great Xing'an Range (between 118°31'30" E to 118°43'20" E and 46°30'30" N to 46°35'00" N) (Fig. 1). The deposit has been mined since 1977, and hosts >250 orebodies of various metals, including Fe, Cu, Pb, Bi, Zn, W–(Mo), Au, Ag, and Ge. Over 150 aeromagnetic anomalies have been detected as potential prospects (Nie et al., 2007; Wang et al., 2014). The Chaobuleng deposit is one of the largest iron-ore deposits in Great Xing'an Range, and it has an estimated ~20 million tonnes of Fe and ~0.4 million tonnes non-ferrous metals (Nie et al., 2007).

The Chaobuleng deposit consists of three primary ore zones in south (Fig. 3A), north, and west (Fig. 2). The NE-trending lens-shaped or stratoid southern zone is ~10 km long and ~3 km wide (Fig. 2). The orebodies are NE-trending in this region, and are hosted in the skarn

along the contact between the Mesozoic intrusion and the Ordovician Tongshan Formation carbonate and slate rocks (Fig. 3A). Mineralization and alteration of the host rocks are most dominant near the margins of the Chaobuleng pluton (Fig. 4A, B, C, D). Skarn and altered hornfels are the major ore types at the Chaobuleng deposit. Hornfels were formed by contact metamorphism caused by intrusion of the Chaobuleng pluton, and include felsic biotite hornfels. In this study, for the southern zone (Fig. 3A), we specifically refer to the host-rock-alteration zones that are immediately adjacent to the pluton and farther away as the inner and outer contact belts, respectively (Fig. 3A). Most ores of the Chaobuleng deposit are massive and disseminated, and are sometimes banded and brecciated (Fig. 3B). All the ores have similar mineral assemblages. Magnetite is the dominant ore mineral, usually accompanied with chalcopyrite, pyrite, sphalerite, galena, and cassiterite (Fig. 4F, G, H, I).

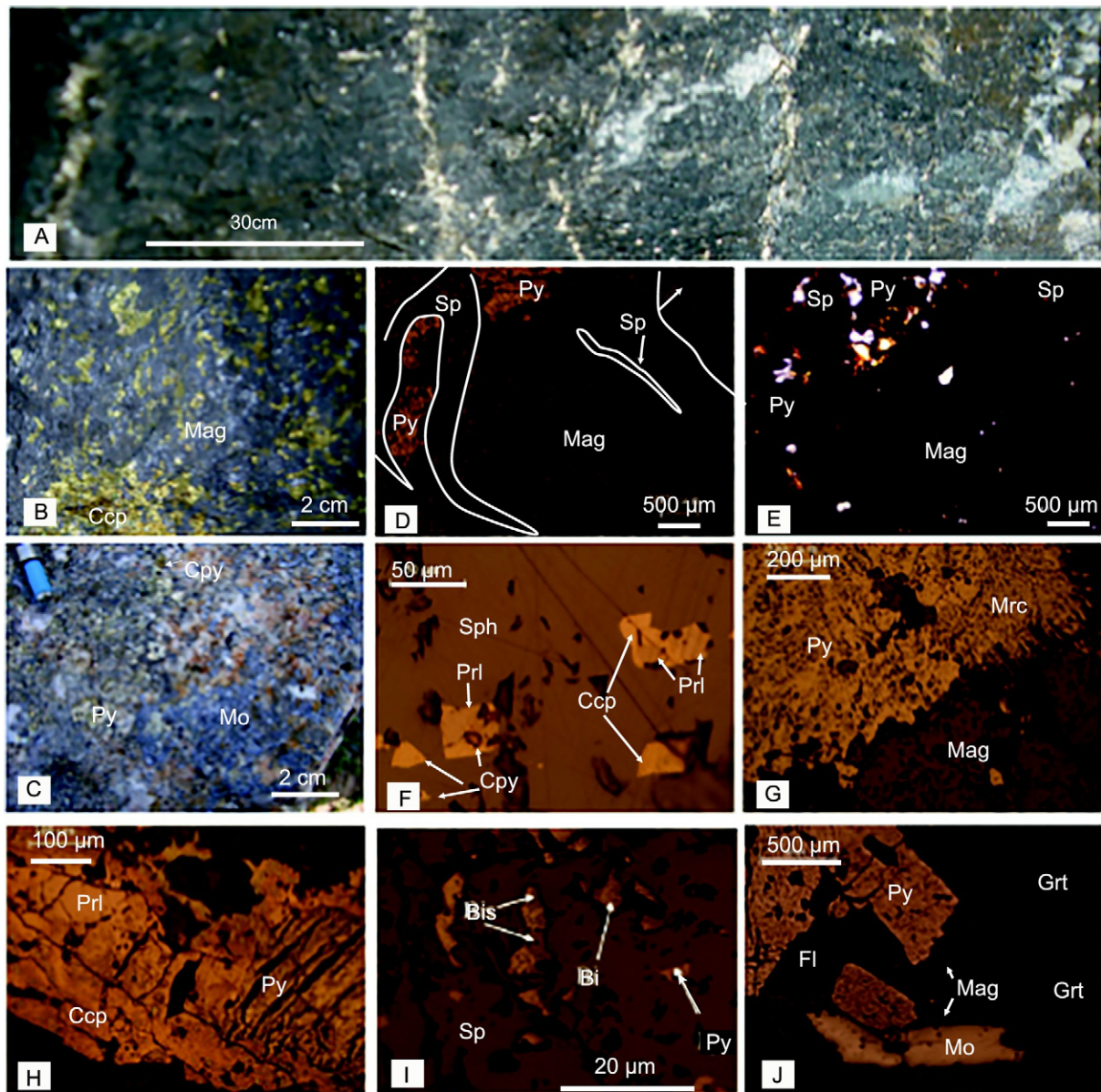


Fig. 5. Photographs showing the textural characteristics of Cu polymetallic sulfide ore from the Chaobuleng iron polymetallic deposit. (A) Sulfide veins cutting hornfels. (B) Chalcopyrite superimposed upon massive iron oxide ore. (C) Fracture plane through a sulfide vein in the granitoid, composed of chalcopyrite pyrite and molybdenite. (D–E) Replacement of magnetite by an assemblage of sphalerite and pyrite, sphalerite with red internal reflection color. (F) Sphalerite including chalcopyrite and minor pyrrhotite. (G) Replacement of magnetite by an assemblage of marcasite and pyrite. (H) Equilibrium between chalcopyrite, pyrite and pyrrhotite. (I) Sphalerite including pyrite and a late assemblage of bismuthinite and bismuth. (J) Late assemblage of pyrite, molybdenite and fluorite superimposed upon garnet and minor magnetite. Py-pyrite; Sp-sphalerite; Mag-magnetite; Mo-molybdenite; Ccp-chalcopyrite; PrI-pyrrhotite; Mrc-marcasite; Bis-bismuthinite; Bi-bismuth; Fl-fluorite; Grt-garnet. (For interpretation of the references to color in this figure legend, the reader is referred to the web version of this article.)

More than 10 ore bodies in the southern and northern zones have been recognized and are spatially and temporally associated with the skarns and hornfels that are found along the contact zone between the Mesozoic intrusion and the Ordovician Tongshan Formation (Figs. 2 and 3A). Iron polymetallic mineralization is dominantly developed

in the SE-trending outer-contact belt, and the iron orebodies extend for over 300 m with a vertical thickness of ~30 m (Fig. 3B). The iron orebodies are hosted in the skarn along the contact between the Ordovician Tongshan Formation sandstones and the carbonate rocks (Fig. 3A). The orebodies are massive, banded, and disseminated throughout

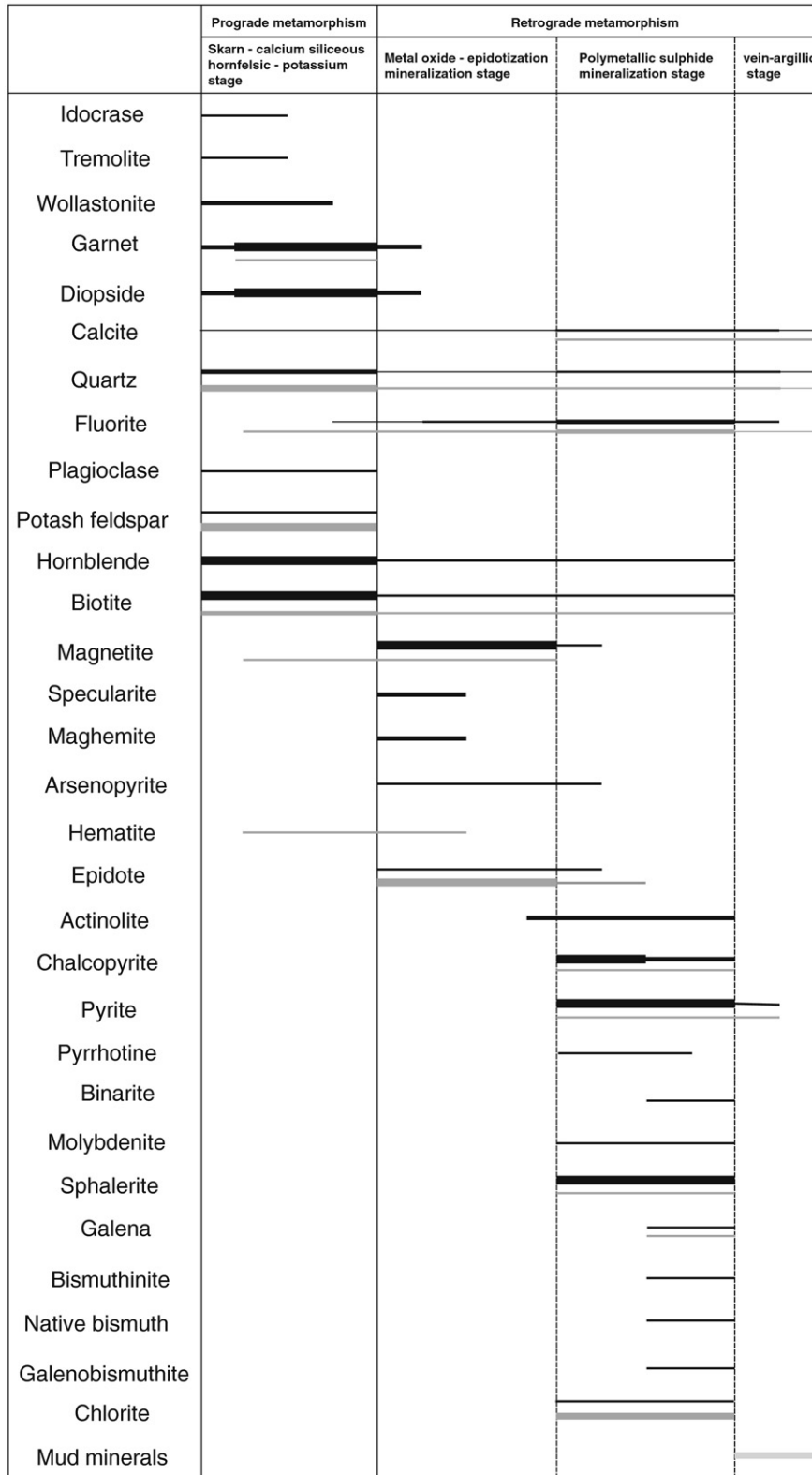


Fig. 6. Episodes and sequence of mineral crystallization in the Chaobuleng iron polymetallic deposit. Gray line for alteration minerals in the margin of the pluton, black line for alteration minerals in the wall rock.

of the mineralization zones (Fig. 3B). Massive magnetites occur along at the contact zone between the Mesozoic intrusion and the skarns (Fig. 4A). The sulfide mineralization, including Cu-Zn-Mo orebodies, are hosted in the skarns and/or Ca-silicate hornfels (Fig. 3A). The sulfide minerals formed within the hosting skarns and Ca-silicate hornfels form as veins that cut through the disseminated iron orebodies (Figs.

4C, 5A). Mineralization of the inner contact belt is rare, and includes minor vein polymetallic sulfides. Cu mineralization occurs in the Ca-hornfels of the western zone that formed in the Ordovician Tongshan Formation sandstones as southeast-trending mesh-veins (Figs. 2, 3A, and 5). The primary Cu orebody extends for over 200 m in length with a vertical thickness of ~4 m (Fig. 3A).

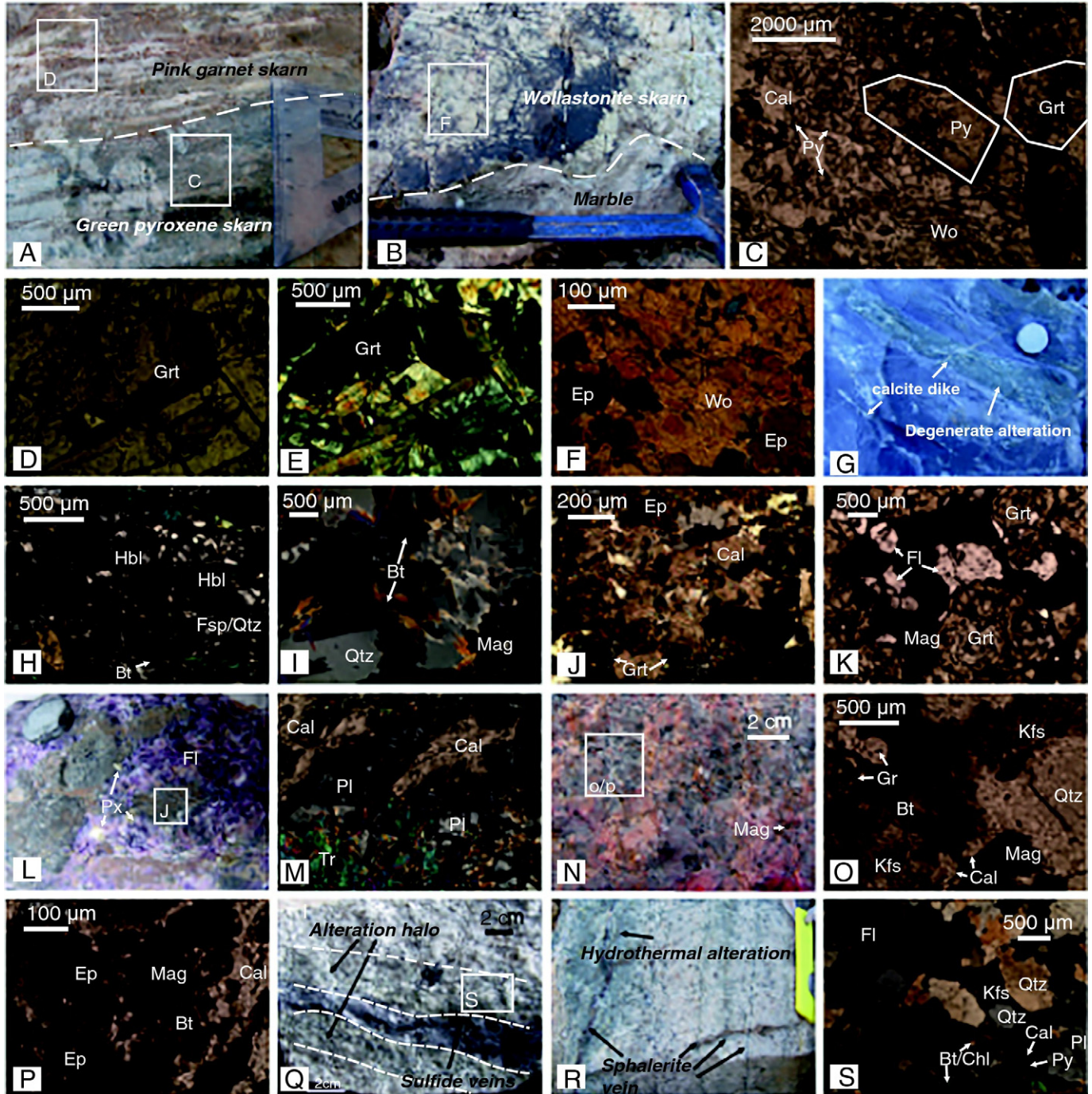


Fig. 7. Alteration type and textural characteristics of the Chaobuleng iron polymetallic deposit. (A–B) Red garnet skarn, green pyroxene skarn, wollastonite skarn, and wollastonite-bearing marble formed in order from pluton to the marginal marble. (C) Green pyroxene skarn, composed of pyroxene, minor garnet, wollastonite and calcite. (D–E) Zoned garnet in the red garnet. (F) Replacement of wollastonite by episode in the wollastonite skarn. (G–H) Hornfels, composed of hornblende, biotite plagioclase and quartz. Retrograde alteration associated with iron oxide mineralization, including (I) assemblage of biotite, quartz and magnetite; (J) assemblage of calcite and episode, with minor residue garnet, and (K) replacement of garnet by an assemblage of magnetite and fluorite. (L–M) Fluorite associated with sulfide mineralization cutting hornfels, and simultaneous retrograde alteration of hornfels, composed of calcite, plagioclase and tremolite. (N–P) Red K-alteration of granite and consequently, a retrograde alteration, the former with an assemblage of biotite, K-feldspar, minor garnet and the latter with an assemblage of magnetite, episode and calcite. (Q–S) Hydrothermal alteration or halo associated with sulfide mineralization, with an assemblage of chlorite, biotite, quartz, fluorite and calcite. Cal-calcites; Px-pyroxene; Gr-garnet; Wo-wollastonite; Epi-episode; Hbl-hornblende; Fsp-feldspar; Bt-biotite; Qtz-quartz; Mag-magnetite; Fl-fluorite; Tr-tremolite; Pl-plagioclase; Py-pyrite; Kfs-K-feldspar; Chl-chlorite. (For interpretation of the references to color in this figure legend, the reader is referred to the web version of this article.)

Hydrothermal alteration is also significant at the contact zone between the Ordovician strata and the Chaobuleng pluton (Fig. 7). The types of hydrothermal alteration include: (1) prograde alteration in the outer contact belt, (2) retrograde alteration and hydrothermal veins associated with iron polymetallic mineralization (Fig. 7I, J, K)

and (3) hydrothermal alteration and hydrothermal veins along the edge of the Chaobuleng pluton (Fig. 6). The prograde alteration occurred during the early stages of the hydrothermal activity, which formed the skarns and Ca-Si hornfels (Fig. 7G, H). These rocks are cross-cut by metasomatic retrograde alteration associated with iron

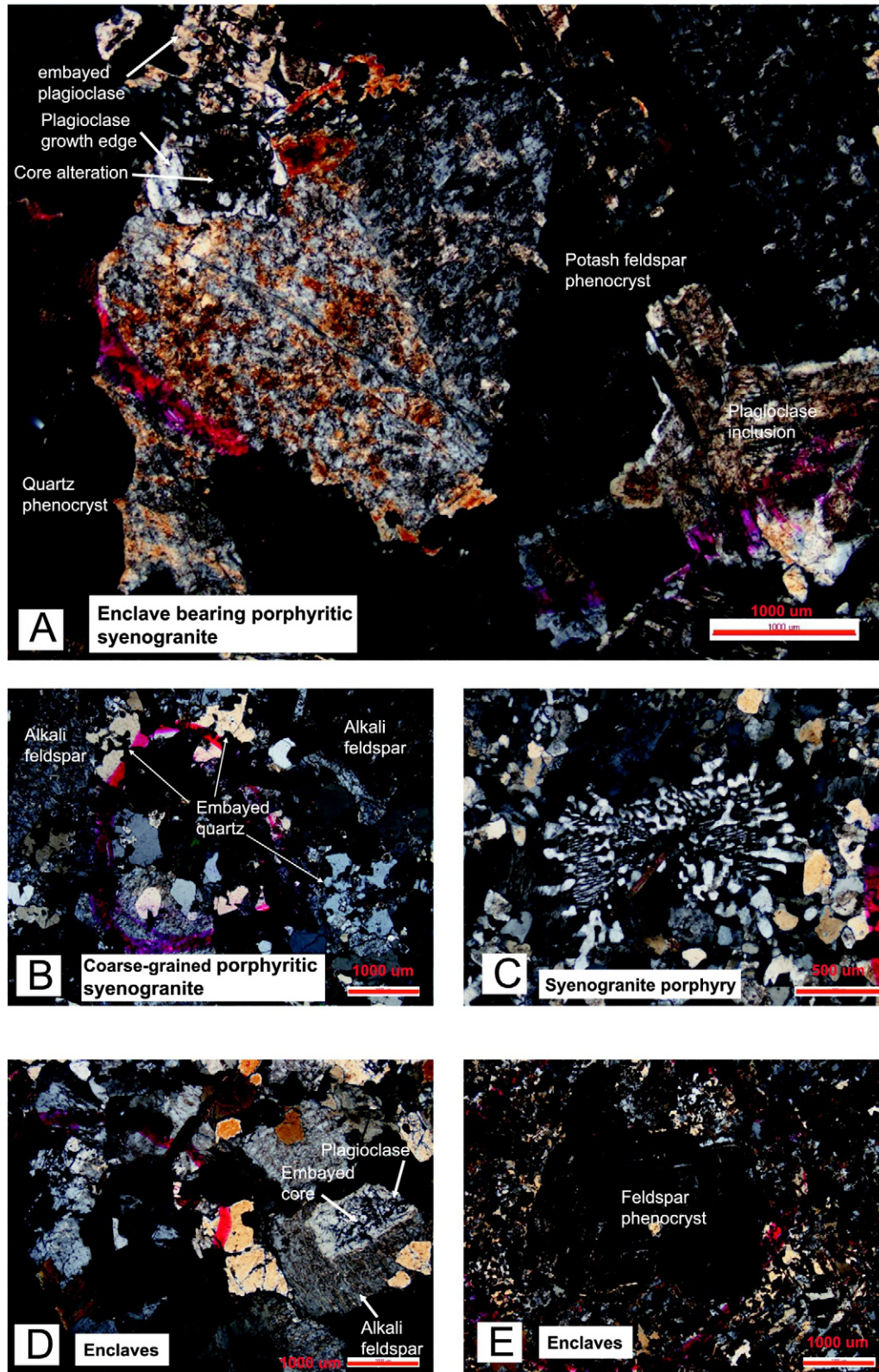


Fig. 8. Microphotographs showing petrography of (A) enclave bearing porphyritic syenogranite, (B) coarse-grained porphyritic syenogranite, (C) syenogranite porphyry, (D–E) enclaves from Chaobuleng pluton.

Table 1
Summary of sample numbers and sample locations.

Sample number	Description	Latitude (°N)	Longitude (°E)	Age
PM109-2	Syenogranite porphyry	46.532	118.542	140.6 ± 1.1 Ma
PM105-3	Syenogranite porphyry	46.51	118.586	138.1 ± 1.1 Ma
PM109-9a	Enclave bearing porphyritic syenogranite	46.534	118.545	138.6 ± 0.91 Ma
PM109-12	Enclave bearing porphyritic syenogranite	46.53	118.541	137.4 ± 1.2 Ma
PM109-9b	Enclave	46.534	118.545	132.6 ± 5.2 Ma
PM109-13	Enclave	46.53	118.541	140.4 ± 4.4 Ma
PM105-1a	Coarse-grained porphyritic syenogranite	46.514	118.545	133.9 ± 1.2 Ma
PM105-1b	Coarse-grained porphyritic syenogranite	46.512	118.544	134.8 ± 0.94 Ma
PM105-1c	Coarse-grained porphyritic syenogranite	46.512	118.547	135.98 ± 0.83 Ma
D8630-1	Coarse-grained porphyritic syenogranite	46.503	118.543	134.4 ± 0.99 Ma
D8334-1	Coarse-grained porphyritic syenogranite	46.515	118.542	133.9 ± 1.2 Ma

polymetallic mineralization (Fig. 7I, J, K). The magnetite orebodies display a sharp contact with the carbonate zone (Figs. 4B, 5B). The skarn-alteration zone consists predominantly of diopside, and subordinate tremolite, albite, mica, chlorite, as well as magnetite, pyrite, chalcocopyrite (Fig. 7A, B, C). Additionally, albitization is generally observed along the margin of the intrusion near the contact zone with the skarn, suggesting post-magmatic hydrothermal process (Fig. 8B). Retrograde alteration associated with iron polymetallic mineralization forms an alteration-mineralization halo. At the metallic oxide mineralization stage, the epidote, calcite, fluorite, quartz, hornblende, biotite grains are made up of the alteration halo that overlapped the skarns (Fig. 7Q, R, S). At the sulfide mineralization stage, hydrosilicate minerals (including pyroxene, garnet, phlogopite, and humite) + quartz + calcite ± fluorite are associated with the sulfides (Fig. 7B, D, E). Quartz and calcite veins are developed after the main mineralization stage (Fig. 7S). Hydrothermal alteration of the margins of the Chaobuleng pluton includes (1) potassium alteration, epidote alteration, and the hydrothermal vein associated with iron polymetallic mineralization during the earlier phase, and (2) argillic alteration during the late phase.

Potassic, epidote, and argillic alteration of the inner contact belt corresponds to the skarn and hornfels, iron sulfide, and hydrothermal vein alteration of the outer contact belt, respectively (Fig. 6). The hydrothermal alteration and mineralization can be divided into two stages. Stage one is characterized by skarns, Ca-Si hornfels, and veins with potassic alteration. The skarn forms the assemblage garnet + pyroxene + wollastonite + calcite + quartz + fluorite + feldspar + magnetite + hematite (Fig. 7A, B, C, and F). The Ca-Si hornfel forms the assemblage hornblende + biotite + feldspar + quartz. The veins are characterized by the assemblage potassium feldspar + biotite + quartz + fluorite + magnetite + hematite (Fig. 7K, L, M). Stage two is characterized by iron oxide mineralization-epidote alteration and sulfide mineralization-argillic alteration (Fig. 7I, J, K). The iron oxide mineralization has the assemblage magnetite + maghemite + specularite + arsenopyrite + epidote + hornblende + boitite + calcite + fluorite. The epidote alteration forms the assemblage epidote + biotite + fluorite + quartz + magnetite + hematite. The sulfide mineralization contains the assemblage chalcocopyrite + pyrrhotite + pyrite + marcasite + sphalerite + gellenite + bismuthinite + native bismuth + fluorite + quartz + biotite + muscovite + hornblende + actinolite + calcite + chlorite + epidote. The quartz and

calcite veins and the argillic alteration along the pluton margin represent the end of the hydrothermal activity.

3. Sampling and analytical methods

3.1. U-Pb zircon dating

Two syenogranite porphyry samples, consisting of plagioclase feldspar, potassium feldspar, quartz, biotite, were collected in this study. Both have the porphyritic textures with <~10% phenocrysts that are mainly composed of potassium feldspar and quartz. Groundmass is ~90% felsic (~50% potassium feldspar, ~20% plagioclase feldspar, and ~20% quartz) with rare biotite. The accessory minerals include magnetite, rutile, monazite, and zircon (Fig. 8C).

Two samples of the enclave bearing porphyritic syenogranite unit consist of plagioclase feldspar (~20%), potassium feldspar (~50%), quartz (~25%), and biotite (<5%). Accessory minerals in these samples include magnetite, titanite, and zircon. Plagioclase feldspar displays a complex zoned texture, which is characterized by hypidiomorphic-idiomorphic boards, polysynthetic twins, and simple double-crystal growth with sizes of 1–4 mm in diameter, and partly shows sericitization and epidotization (Fig. 8A). Two fine-grain enclave samples (Fig. 8D, E) are the dark gray granodiorite that consist of plagioclase feldspar (~60%), potassium feldspar (~15%), quartz (~20%), and biotite (~5%). Accessory minerals include magnetite and titanite.

Five coarse-grained porphyritic syenogranite samples consist of plagioclase feldspar (~30%), potassium feldspar (~50%), quartz (~20%), and rare biotite. The plagioclase appears as hypidiomorphic boards, polysynthetic twins with sizes of 0.5–2.0 mm in diameter. These samples show minor sericitization. The accessory minerals include zircon and apatite (Fig. 8B).

Mineral separation was conducted at the Institute of the Hebei Regional Geology and Mineral Survey in Langfang, China. Samples were crushed to pass a 60-mesh sieve and were then manually washed by water and alcohol. We used an electromagnetometer to remove magnetic minerals and a heavy liquid to concentrate heavy minerals. Zircon grains were then handpicked under a binocular microscope. Zircon grains from individual samples were mounted in epoxy resin and polished close to one-third of individual grain diameters. Cathodoluminescence (CL) imaging was employed to investigate the

Table 2
Results of Re-Os isotopic analyses of molybdenite samples from the Chaobuleng iron polymetallic deposit.

Sample number	Sample weight	Re (µg/g)	¹⁸⁷ Os (µg/g)	Model age (Ma)	Data source
CBL6-1	0.01778	3781 ± 34	5.512 ± 0.041	139.0 ± 2.0	Nie et al., 2007
CBL6-2	0.0133	8520 ± 88	12.580 ± 0.10	140.9 ± 2.1	Nie et al., 2007
CBL6-3	0.01028	9272 ± 77	13.53 ± 0.10	139.2 ± 1.9	Nie et al., 2007
CBL6-4	0.01917	14,024 ± 139	20.65 ± 0.15	140.5 ± 2.0	Nie et al., 2007
6TW1	0.01663	7230 ± 68	10.152 ± 0.11	135.0 ± 2.1 Ma	This study
Mo-1	0.01558	4113 ± 43	8.635 ± 0.093	131.2 ± 4.1 Ma	This study

internal texture of zircon, which in turn was used for selecting appropriate spots for U–Pb dating. Zircon analysis of these samples was performed on the Neptune multiple collector inductively coupled plasma mass spectrometer (Thermo Fisher Ltd.) with a 193-nm-FX Ar Excimer laser-ablation system (ESI Ltd.) at the Isotopic Laboratory, Tianjin Institute of Geology and Mineral Resources. NIST610 glass was used as an external standard to calculate U, Th, Pb concentrations of zircons, common Pb correction used the ^{208}Pb method (Andersen, 2002), and TEMORA zircon (Black et al., 2003) was used as an external standard to normalize isotopic fractionation during the analysis. The locations of these samples

are presented in Table 1, and detailed analytical results are reported in Table A1 in the Supplementary data.

3.2. Geochemical analyses of igneous rocks

Major oxides of samples were analyzed by X-ray fluorescence analysis (XRF; PHILIPS PW1480) using fused glass disks at the National Research Center for Geoanalysis, Chinese Academy of Geological Sciences (CAGS) in Beijing, China. The analytical uncertainties are <1%, estimated from repeated analyses of two standards (andesite GSR-2 and basalt

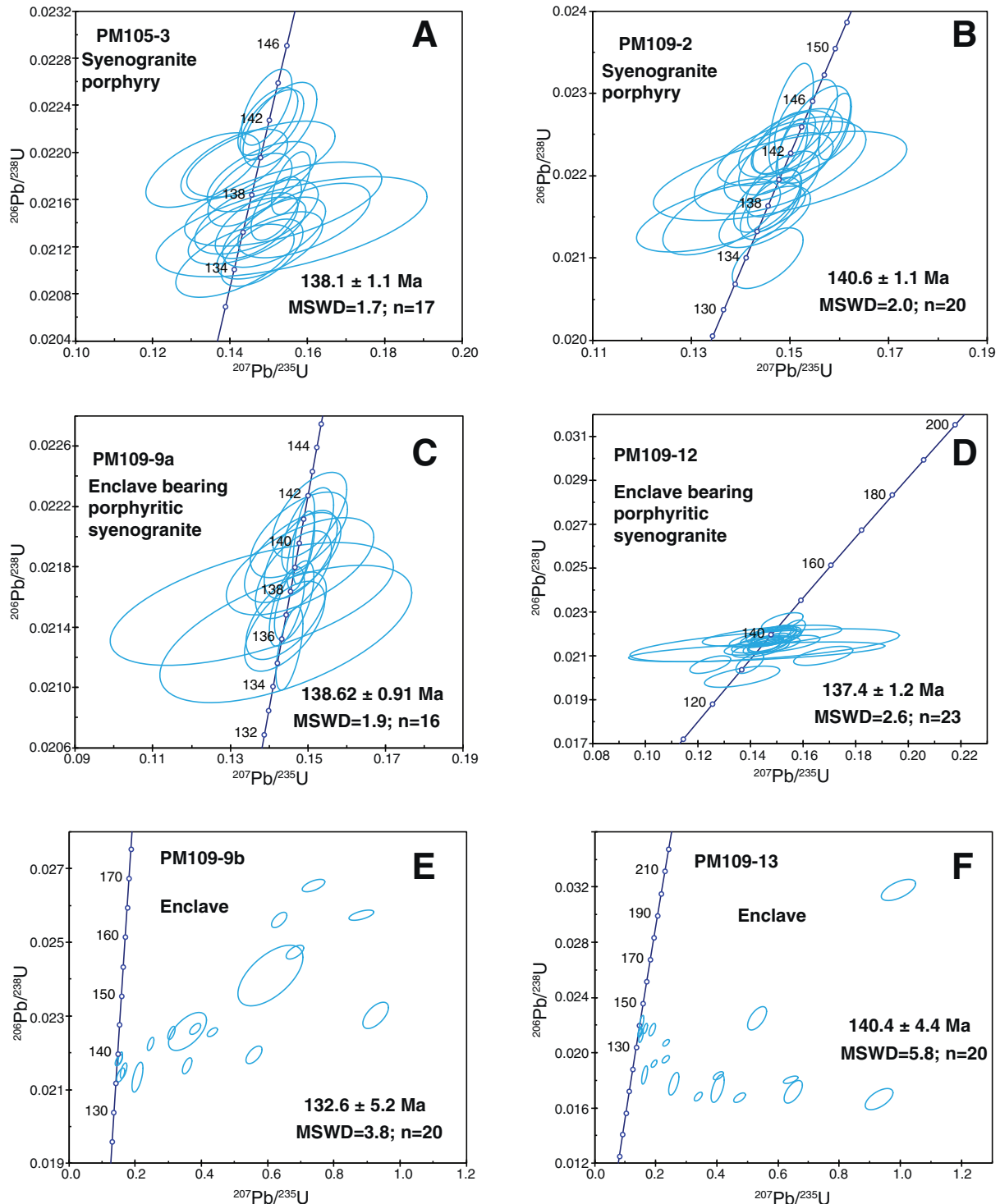


Fig. 9. Zircon $^{207}\text{Pb}/^{235}\text{U}$ - $^{206}\text{Pb}/^{238}\text{U}$ concordia diagrams of granitic samples collected from the Chaobuleng pluton. MSWD—mean square of weighted deviates.

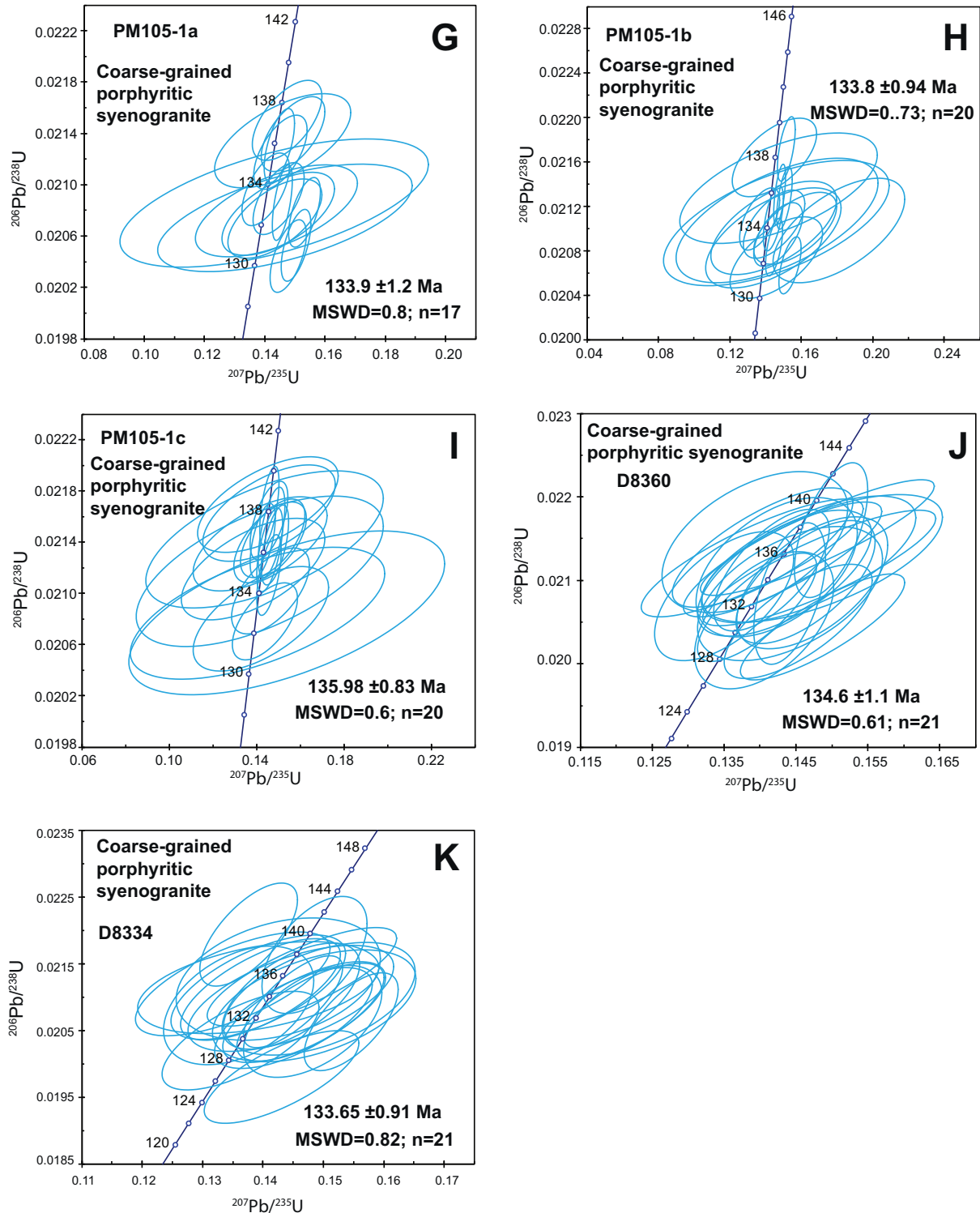


Fig. 9 (continued).

GSR-3). Loss on ignition was determined gravimetrically after heating the samples at 980 °C for 30 min. Uncertainties for most major oxides are <2 wt%, for MnO and P₂O₅ < 5 wt%, and the totals are within 100 ± 1 wt%.

Trace element analyses were determined by inductively coupled plasma mass spectrometry (ICP-MS) hosted in the National Research Center for Geoanalysis, Chinese Academy of Geological Sciences (CAGS) in Beijing, China. Precision for most elements was typically better than 5% RSD (relative standard deviation), and the measured values

for Zr, Hf, Nb, and Ta were within 10% of the certified values. The sample preparation, instrument operating conditions, and calibration procedures follow those established by Liang et al. (2000). Two standards (granite GSR-1, basalt GSR-3) were used to monitor the analytical quality. The analytical errors vary from 3 to 7% depending on the concentration of any given element. An internal standard was used for monitoring drift during analysis. The further details have been given by Gao et al. (2008). The detailed geochemical results are reported in Table A2 in the Supplementary data.

3.3. Re–Os molybdenite dating

Two molybdenite samples were collected for Re–Os dating from the inner contact belt of the northern zone (Fig. 2), which show the chlorite alteration mineral halo. The ore samples are euhedral to subhedral, which developed as massive veins in the mineralized coarse-grained syenogranite porphyry with pyrite, bismuthine, and quartz. Gravity and magnetic separations were followed by handpicking of molybdenite grains under a binocular microscope (purity > 99%). Fine-grained (<0.1 mm) molybdenite grains were selected to avoid the effects of decoupling Re and Os within large molybdenite grains (Stein et al., 2003; Selby and Creaser, 2004). Re–Os isotope analysis was performed in the Re–Os Laboratory, Institute of Geology and Mineral Resources in Tianjin, China using an ICP-MS (TJA X-series; Thermo Electron Corporation, Waltham, MA, USA). The analytical procedures of Shirey and Walker (1995) were followed. Model ages were calculated following the equation: $t = [\ln(1 + \frac{^{187}\text{Os}}{^{187}\text{Re}})]/\lambda$, where λ is the decay constant of ^{187}Re , $1.666 \times 10^{-11} \text{ year}^{-1}$ (Smoliar et al. 1996). The detailed data are presented in Table 2.

3.4. Mineral chemistry

Microprobe analyses of plagioclase and biotite were performed by wavelength dispersive analysis (WDP) using standard procedures on the EPMA-1600 Superprobe at the State Key Laboratory of Geological Process and Mineral Resources of the China University of Geosciences, Beijing. Electron microprobe analyses were carried out on those minerals under the following operating conditions: 15 kV accelerating voltage, 10 nA beam current and 1–5 μm beam diameter. Data were corrected using the ZAF correction procedure after Armstrong (1995). Measurement precision is better than 1 wt% for the element oxides.

4. Analysis results

4.1. U–Pb zircon ages of igneous samples

Analytical data from the U–Pb zircon dating can be found in Table A1 in the Supplementary data. Zircon grains chosen for this study were euhedral and prismatic in shape and ~100–150 μm long. The length-to-width ratios of dated zircon grains were typically 2:1–3:1. A few grains show elongate length/width ratios of 4:1. Most of the dated zircon grains were transparent and colorless under the optical microscope, although some appeared brownish, possibly due to high U contents. Zircon grains display both concentric zoning and inherited cores with magmatic overgrowth rims. Uncertainties of individual analyses are reported with 1σ errors; weighted mean ages are reported at the 2σ confidence level. Age calculations and concordia plots were made using Isoplot (Ludwig, 2003). In total, 300 zircons were analyzed, and the analytical results in the form of concordia diagrams are presented in Fig. 9. Most analyses are concordant or nearly concordant, clustering as single age populations. To eliminate the effects of radiation damages (typically displayed by dark CL images indicating high U contents), Pb loss, and erroneous analyses, we used only the ages that clearly belonged the same Gaussian distribution for calculating the weighted mean ages of pluton emplacement (e.g., Dai et al., 2013). Their weighted mean $^{206}\text{Pb}/^{238}\text{U}$ ages are interpreted to represent the crystallization age of the plutons from which the samples were collected. Although the Th/U ratios and crystal morphology suggest that all zircon grains have a magmatic origin (Vavra et al., 1996; Harley et al., 2007), there are a few zircons that have low Th/U ratios (<0.1) (see the Table A1 in the Supplementary data).

4.1.1. Syenogranite porphyry

Samples PM109-2 and PM105-3 were both collected from the syenogranite porphyry unit of the Chaobuleng pluton. Sixteen analyses of sample PM105-3 yield a weighted mean $^{206}\text{Pb}/^{238}\text{U}$ age of $138.1 \pm 1.1 \text{ Ma}$ (MSWD = 1.7; Fig. 9A), which we interpret as the crystallization age of this syenogranite porphyry sample. The $^{206}\text{Pb}/^{238}\text{U}$ ages of 20 analyses from sample PM109-2 yield a weighted mean $^{206}\text{Pb}/^{238}\text{U}$ age of $140.6 \pm 1.1 \text{ Ma}$ (MSWD = 2.0, $n = 20$) (Fig. 9B), which is interpreted as the crystallization age of this sample.

4.1.2. Enclave bearing porphyritic syenogranite

Both samples PM109-9a and PM109-12 are enclave bearing porphyritic syenogranites collected from the Chaobuleng pluton. Sixteen analyses from sample PM109-9a yield a weighted mean $^{206}\text{Pb}/^{238}\text{U}$ age of $138.6 \pm 0.91 \text{ Ma}$ (MSWD = 1.9; Fig. 9C), which we interpret to represent the crystallization age of the sample. The $^{206}\text{Pb}/^{238}\text{U}$ analyses of 23 grains from sample PM109-12 yield a weighted mean $^{206}\text{Pb}/^{238}\text{U}$ age of $137.4 \pm 1.2 \text{ Ma}$ (MSWD = 2.6, $n = 23$) (Fig. 9D), which we interpret to represent the crystallization age of the enclave bearing porphyritic syenogranite sample. Enclave samples PM109-9b and PM109-13 are granodiorites. The $^{206}\text{Pb}/^{238}\text{U}$ ages of the two enclave samples yield a weighted mean $^{206}\text{Pb}/^{238}\text{U}$ age of ~138 Ma, although many of the analyses are discordant and probably show the effects of significant Pb loss (Fig. 9E, F).

4.1.3. Coarse-grained porphyritic syenogranite

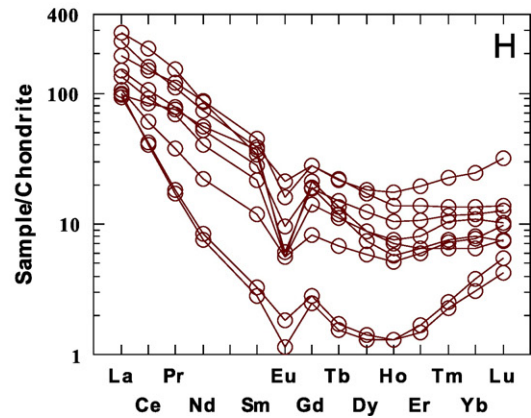
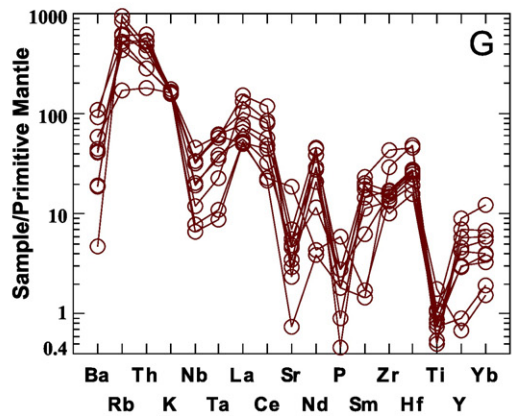
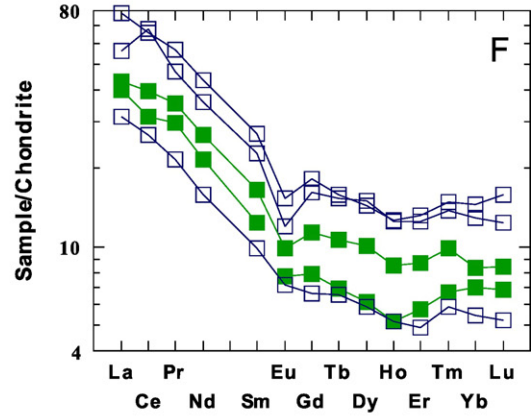
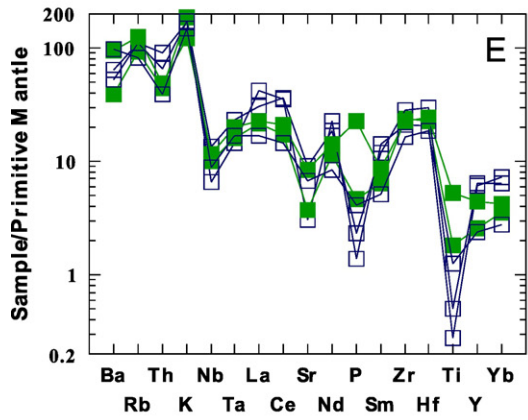
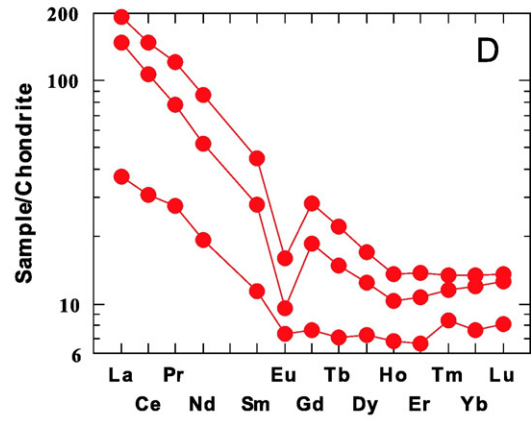
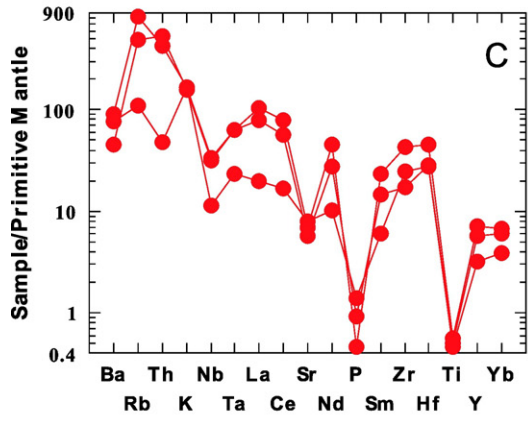
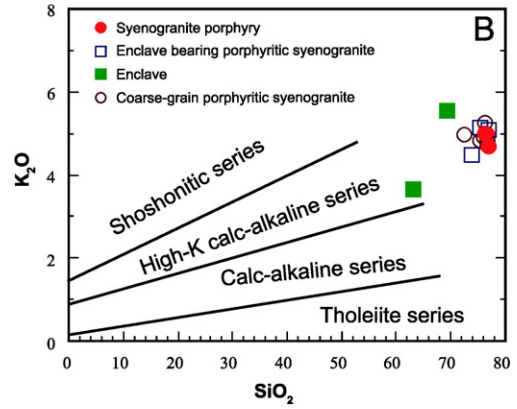
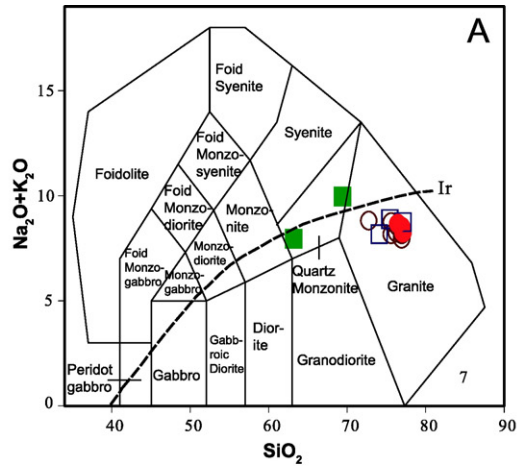
Five coarse-grained porphyritic syenogranite samples were collected from the center of the Chaobuleng pluton. The weighted mean $^{206}\text{Pb}/^{238}\text{U}$ zircon ages of samples PM105-1a, PM105-1b, PM105-1c, D8630-1, D8334-1, determined from 17, 20, 20, 21, and 21 zircon-grain analyses respectively, were $133.9 \pm 1.2 \text{ Ma}$ (MSWD = 0.8) (Fig. 9G), $134.8 \pm 0.94 \text{ Ma}$ (MSWD = 0.73) (Fig. 9H), $135.98 \pm 0.83 \text{ Ma}$ (MSWD = 0.6) (Fig. 9I), $134.4 \pm 0.99 \text{ Ma}$ (MSWD = 0.61) (Fig. 9J), and $133.9 \pm 1.2 \text{ Ma}$ (MSWD = 0.82) (Fig. 9K) respectively. We interpret these mean ages as the crystallization ages of the coarse-grained porphyritic syenogranite samples. We suggest an overall average age of 134.6 Ma for this unit.

4.2. Major- and trace-element compositions of the igneous samples

Three syenogranite porphyry samples were analyzed for major- and trace-element compositions. Oxide contents range from 76.5 to 77.04 wt% for SiO_2 , 8.25 to 8.65 wt% for $(\text{K}_2\text{O} + \text{Na}_2\text{O})$, 0.36 to 0.64 wt% for Fe_2O_3 , 0.14 to 0.22 wt% for FeO, 0.10 to 0.11 wt% for MgO, lower content 12.08 to 12.39 wt% for Al_2O_3 , and the ratio values of $\text{K}_2\text{O}/\text{Na}_2\text{O}$ are 1.33 to 1.42 (see the Table A2 in the Supplementary data). The samples are weakly peraluminous, as indicated by molar $A/\text{CNK} = 1.01\text{--}1.05$ (Maniar and Piccoli, 1989). The analyzed samples are classified as granite on the $(\text{K}_2\text{O} + \text{Na}_2\text{O})$ versus SiO_2 plot (Fig. 10A; Middlemost, 1994). In the K_2O versus SiO_2 diagram (Le Maitre et al., 1989; Rickwood, 1989), all samples plot in the field of the high-potassium calc-alkaline series (Fig. 10B; Le Maitre et al., 1989; Rickwood, 1989).

Based on trace-element measurements from these samples (Table A2 in the Supplementary data), the multi-element diagram normalized by the primitive-mantle composition shows enrichment in large ion lithophile elements (LILEs, such as Ba, Rb, K) and depletion in high field strength elements (HFSEs, such as Nb, Ta, Sr, Ti, and P; Fig. 10C). The REE abundances of each sample, normalized by chondrite values of Sun and McDonough (1989), are variable. All samples display enriched light rare-earth element (LREE) and flat heavy rare-earth

Fig. 10. (A) SiO_2 – $(\text{K}_2\text{O} + \text{Na}_2\text{O})$ (total alkali–silica [TAS]) diagram for intrusive rocks. Normalization values are from Middlemost (1994). (B) K_2O vs. SiO_2 diagram for intrusive rocks. Normalization values are from Le Maitre et al. (1989) and Rickwood (1989). (C, E, G) Primitive mantle–normalized spider diagrams for Chaobuleng granitoid samples. Normalization values are from Sun and McDonough (1989). (D, F, H) Chondrite-normalized rare earth element (REE) diagrams for Chaobuleng granitoid samples. Normalization values are from Boynton (1984).



element (HREE) profiles without distinct Ce anomalies (Fig. 10D). The samples display an obvious negative Eu anomaly ($\delta\text{Eu} = 0.4\text{--}0.5$) (Fig. 10D), with the $(\text{La}/\text{Yb})_N$, $(\text{La}/\text{Gd})_N$, $(\text{Gd}/\text{Yb})_N$ ratios of 12.4–14.3, 6.9–7.9, 1.6–2.1 (where N denotes normalized to chondrite values of Sun and McDonough [1989]).

Four enclave bearing porphyritic syenogranite samples and two enclave samples were analyzed for major- and trace-element compositions. Oxide contents of the enclave bearing porphyritic syenogranite samples range from 74.04 to 77.16 wt% for SiO_2 , 8.15 to 8.88 wt% for $(\text{K}_2\text{O} + \text{Na}_2\text{O})$, 0.36 to 1.73 wt% for Fe_2O_3 , 0.21 to 0.46 wt% for FeO, 0.07 to 0.35 wt% for MgO, 12.04 to 13.04 wt% for Al_2O_3 , and the $\text{K}_2\text{O}/\text{Na}_2\text{O}$ ratios are 1.24 to 1.40 (Table A2 in the Supplementary data). The analyzed samples are classified as granite on the $(\text{K}_2\text{O} + \text{Na}_2\text{O})$ versus SiO_2 plot (Fig. 10A; Middlemost, 1994). In the K_2O versus SiO_2 diagram (Le Maitre et al., 1989; Rickwood, 1989), three samples plot in the field of the high-potassium calc-alkaline series (Fig. 10B; Le Maitre et al., 1989; Rickwood, 1989). Oxide contents of two enclave samples range from 63.2 to 69.4 wt% for SiO_2 , 7.98 to 10.0 wt% for $(\text{K}_2\text{O} + \text{Na}_2\text{O})$, 1.57 to 3.31 wt% for Fe_2O_3 , 0.86 to 1.89 wt% for FeO, 0.05 to 1.68 wt% for MgO, relatively higher contents of 14.86 to 15.52 wt% for Al_2O_3 , and the $\text{K}_2\text{O}/\text{Na}_2\text{O}$ ratios are 1.24 to 1.40 (Table A2 in the Supplementary data). The samples are also weakly peraluminous, as indicated by molar $\text{A}/\text{CNK} = 0.95\text{--}0.97$ (Maniar and Piccoli, 1989). The analyzed samples can be classified as quartz monzonite on the $(\text{K}_2\text{O} + \text{Na}_2\text{O})$ versus SiO_2 plot (Fig. 10A; Middlemost, 1994). In the K_2O versus SiO_2 diagram (Le Maitre et al., 1989; Rickwood, 1989), three samples plot in the field of the high-potassium calc-alkaline series (Fig. 10B; Le Maitre et al., 1989; Rickwood, 1989).

The trace-element characteristics of the enclave samples (Table A2 in the Supplementary data) are similar to the enclave bearing porphyritic syenogranite samples. For these samples, the multi-element diagram normalized by the primitive-mantle composition shows enrichment in large ion lithophile elements (LILEs, such as Ba, Rb, K) and depletion in high field strength elements (HFSEs, such as Nb, Ta, Sr, Ti, P; Fig. 10E). The samples display variable REE abundances normalized by chondrite values of Sun and McDonough (1989). All samples displayed enriched light rare-earth element (LREE) and flat heavy rare-earth element (HREE) profiles without distinct Ce anomalies (Fig. 10F). The samples show a weaker negative Eu anomaly ($\delta\text{Eu} = 0.6\text{--}0.9$) relative to enclave bearing porphyritic syenogranite samples (Fig. 10F), with the $(\text{La}/\text{Yb})_N$ ratios of 4.4–5.8.

Eight coarse-grained porphyritic syenogranite samples were analyzed for major- and trace-element compositions. Oxide contents range from 72.74 to 76.94 wt% for SiO_2 , 8.18 to 8.79 wt% for $(\text{K}_2\text{O} + \text{Na}_2\text{O})$, 0.77 to 1.68 wt% for Fe_2O_3 , 0.24 to 0.74 wt% for FeO, 0.25 to 0.57 wt% for MgO, relatively lower concentrations of 11.82 to 13.35 wt% for Al_2O_3 , and the ratio values of $\text{K}_2\text{O}/\text{Na}_2\text{O}$ are 1.24 to 1.62 (Table A2 in the Supplementary data). The samples are weakly peraluminous, as indicated by molar $\text{A}/\text{CNK} = 0.97\text{--}1.06$ (Maniar and Piccoli, 1989). The analyzed samples are classified as granite on the $(\text{K}_2\text{O} + \text{Na}_2\text{O})$ versus SiO_2 plot (Fig. 10A; Middlemost, 1994). In the K_2O versus SiO_2 diagram (Le Maitre et al., 1989; Rickwood, 1989), all samples plot in the field of the high-potassium calc-alkaline series (Fig. 10B; Le Maitre et al., 1989; Rickwood, 1989).

Trace-element data from the coarse-grained porphyritic syenogranite samples (Table A2 in the Supplementary data) plotted on a multi-element diagram normalized by the primitive-mantle composition shows enrichment in large ion lithophile elements (LILEs, including Ba, Rb, K) and depletion in high field strength elements (HFSEs, such as Nb, Ta, Sr, Ti, P; Fig. 10C). The REE abundances normalized by chondrite values of Sun and McDonough (1989) vary

from sample to sample. All samples displayed enriched light rare-earth element (LREE) and flat heavy rare-earth element (HREE) profiles without distinct Ce anomalies (Fig. 10G). The samples display a clear negative Eu anomaly ($\delta\text{Eu} = 0.2\text{--}0.6$) (Fig. 10H), with the $(\text{La}/\text{Yb})_N$, $(\text{Gd}/\text{Yb})_N$ ratios of 10.1–35.8, 0.7–3.3 (where N denotes normalized to chondrite values of Sun and McDonough (1989)). The negative Ba, Sr, P, and Ti depletions are commonly associated with removal of feldspar, apatite, and ilmenite from felsic melts during crystal fractionation (e.g., Rollinson, 2014).

Most of the Chaobuleng pluton samples plot in the field of A-type granites (Fig. 11A, B), which are generally associated with an extensional settings regardless of the origin of the magma source (e.g., Whalen et al., 1987; Eby, 1990, 1992; Turner et al., 1992). In contrast, the rest of the samples plotted in the field of I-type or S-type of granites, which are commonly associated with arc magmatism and crustal anatexis (e.g., Whalen et al., 1987; Eby, 1990, 1992; Turner et al., 1992; Fig. 11A, B). Discrimination diagrams allow further refinement of the assigned tectonic environments for the Chaobuleng pluton. In the Rb versus $(\text{Y} + \text{Nb})$ and Nb versus Y diagrams (Pearce et al., 1984; Pearce, 1996), the Chaobuleng granitoid samples plotted in the triple junction region of the volcanic-arc, collision-orogen, and within-plate fields (Fig. 11C and D). In the Al_2O_3 versus SiO_2 and $\text{FeO}/(\text{FeO} + \text{MgO})$ versus SiO_2 diagrams (Frost and Frost, 1997), they plot in the post orogenic granite field (Fig. 11E and F), whereas the same samples plot in the late-orogenic field in the R2 versus R1 diagram (Batchelor and Bowden, 1985) (Fig. 11G).

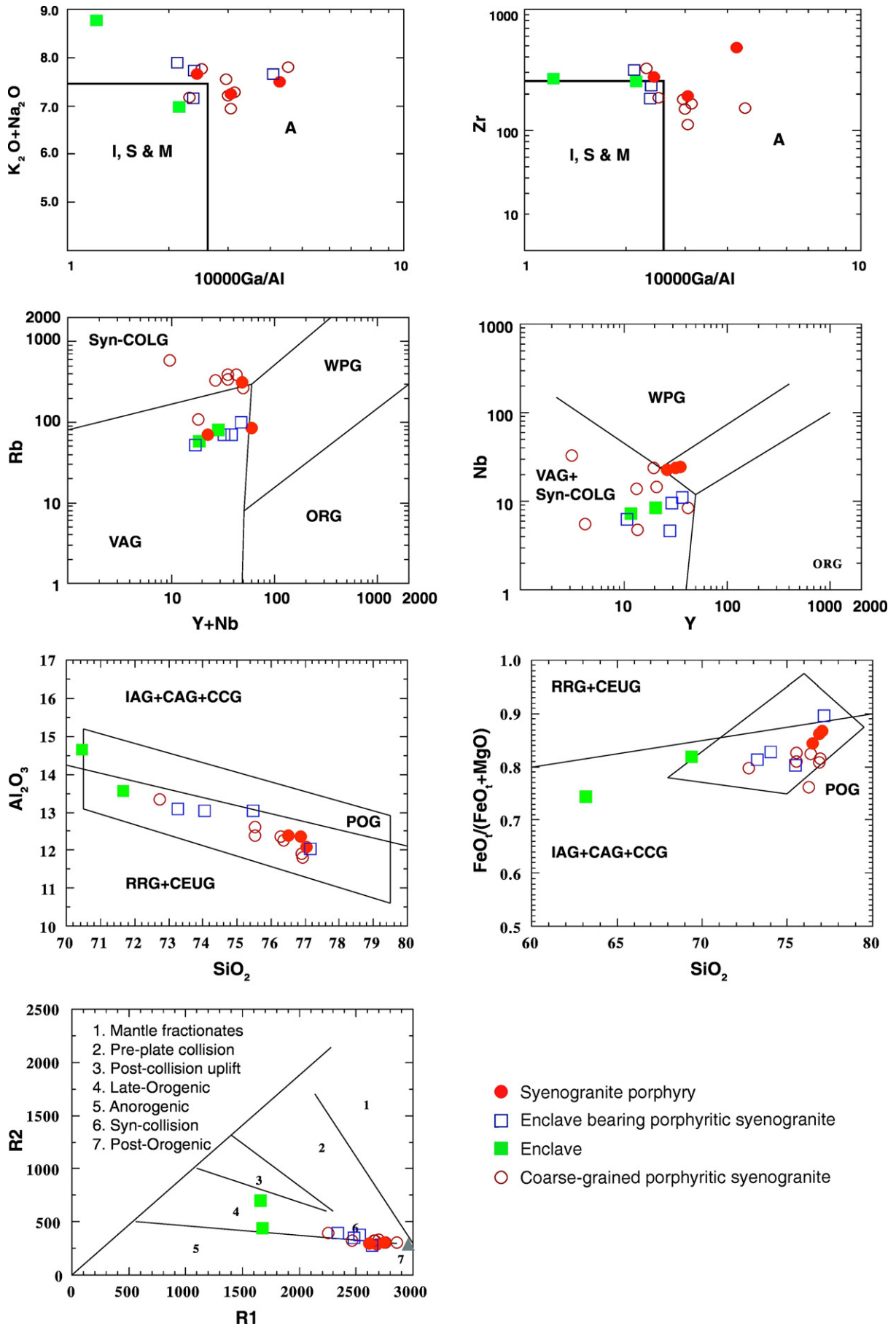
4.3. Re-Os molybdenite dating results

Our molybdenite Re–Os dating results (samples 6TW1 and Mo-1) from the inner contact belt, combined with previously published Re–Os data, are listed in Table 2. From our analyses, the concentrations of Re and ^{187}Os range from 3781 to 14,024 ppm and 5.512 to 20.65 ppb, respectively. The Re–Os model ages of samples 6TW1 and Mo-1 are 135.0 ± 2.1 Ma (1σ) and 131.2 ± 4.1 Ma (1σ), respectively. Using the ISOPLOT/Ex program (Ludwig, 2004), we reinterpreted data of Nie et al. (2007) from the outer contact belt, which yielded an isochron age of 140.7 ± 1.8 Ma (MSWD = 1.12) and an initial $^{187}\text{Os}/^{188}\text{Os}$ ratio of -0.07 ± 0.12 (Fig. 12).

4.4. Mineral chemistry

The compositions of representative plagioclase and biotite grains are presented in Figs. 13 and 14. The plagioclase feldspar can be classified as albite ($\text{An} = 5\text{--}10$) for the syenogranite porphyry, whereas the enclave bearing porphyritic syenogranite and the coarse-grained porphyritic syenogranite have higher plagioclase An-values of 10–20. Plagioclase feldspars from the enclave samples have $\text{An} = 10\text{--}40$. Albite can be recognized in some samples from the Chaobuleng pluton which can be attributed to alteration (Fig. 13A).

Samples from the Chaobuleng pluton contain accessory minerals that include biotite, iron oxide (magnetite, magnetilmenite), zircon, titanite, and Ag-bearing rare earth minerals. The analyzed biotite grains are dominantly magnesian biotite, but the secondary biotite is classified as iron-biotite (Fig. 13B). The $\text{Fe}^\#$ values ($\text{Fe}^\# = \text{Fe}/\text{Fe} + \text{Mg}$ of biotite grains) (Fig. 14) range from 0.25 to 0.45. Both the primary biotite of the Chaobuleng granitoid and secondary biotite show enriched Fe, which represent higher oxidation conditions (Stone, 2000). The F contents of representative analyses of biotite grains range from 1.5% to 3.6%. However, the contents of Fe and F show an inverse trend (Fig. 14).



5. Discussion

5.1. Timing of magma emplacement and mineralization

The Chaobuleng granitoid samples can be characterized into three distinct U-Pb zircon age groups: (1) 138.1–140.6 Ma for the syenogranite porphyry, (2) 137.4–138.6 Ma for the enclave bearing porphyritic syenogranite, and (3) 133.9–135.98 Ma for the coarse-grained porphyritic syenogranite (Fig. 15). The U-Pb zircon age spectrum of the Chaobuleng pluton ranges from 128 Ma to 150 Ma and displays a prominent peak at 130–145 Ma, which represents the best overall estimate for the emplacement ages. The analyses of zircon rims from all of the granitoid samples yielded a concordant mean $^{206}\text{Pb}/^{238}\text{U}$ age of 137.07 ± 0.57 Ma. We interpret this age to best represent the crystallization age of the Chaobuleng pluton. The Re–Os isochron age of the molybdenite from the Chaobuleng deposit is 131.1 ± 3.4 Ma, which is consistent with the intrusion timing of the Early Cretaceous granitoids.

Re–Os isotopic age dating of four molybdenite separates from the outer contact belt yields an isochron age of 140.7 ± 1.8 Ma and model ages that range from 139.0 to 140.0 Ma with an average of 139.5 Ma. The Re–Os isochron age corroborates field observations of molybdenite coexisting with chalcopyrite and pyrrhotite (Fig. 5A, C, J), which suggests that the molybdenite developed at the early stage of the polymetallic sulfide mineralization. Prograde alteration of outer contact belt is distributed along the margin of the syenogranite porphyry and the skarns show obvious zonation features. Thus, we suggest that the emplacement of the syenogranite porphyry caused the observed prograde alteration.

Our new Re–Os isotopic age dating of two molybdenite separates from inner contact belt yields two ages of 135.0 ± 2.1 Ma and 131.2 ± 4.1 Ma. The molybdenite of the inner contact belt formed in a polymetallic sulfide vein that developed in the enclave bearing porphyritic syenogranite and coarse-grained porphyritic syenogranite units. The molybdenite is observed to coexist with pyrite, bismuthinite and quartz (Fig. 5C). This may indicate that the sulfide vein of inner contact belt developed during the later stage of polymetallic sulfide mineralization, related to the intrusion of the coarse-grained porphyritic syenogranite. Based on field observations and petrological evidence, we suggest that the major ore-forming iron-polymetallic mineralization in the skarn rocks occurred during the early stage of the magmatic hydrothermal activities related to the emplacement of the syenogranite porphyry, whereas the main mineralization occurred at the late stage of magmatic activities (e.g., Halliday, 1980).

5.2. Petrogenesis of the Chaobuleng pluton

5.2.1. Pressure and temperature estimates

The estimated zircon saturation temperature (T_{Zr}) can place an upper limit on magma temperature (Miller et al., 2003). In contrast, absence of inherited zircon is consistent with under saturation at the source. Magmatic rocks lacking evidence for inherited or early-crystallizing zircon (i.e., inheritance-poor granitoids) reflect zircon-under saturated melt compositions. Therefore, T_{Zr} provides a minimum estimate for magma temperature at the source before extensive crystallization, probably during initial emplacement (Miller et al., 2003). Based on the zircon saturation experiments of Watson and Harrison (1983) and Boehnke et al. (2013), zircon saturation temperature (T_{Zr}) was established as the following relationship between zircon solubility, temperature, and major element composition of melt:

$$\ln D^{\text{Zr, zircon/melt}} = \{-3.80 - [0.85 \times (M - 1)]\} + 12,900/T \quad (1)$$

where $D^{\text{Zr, zircon/melt}}$ is the concentration ratio of Zr (ppm) in stoichiometric zircon to that in the saturated melt, T is the absolute temperature (all temperatures referred to in this paper have been converted to °C), and M is the cation ratio $(\text{Na} + \text{K} + 2 \times \text{Ca})/(\text{Al} + \text{Si})$. The zircon

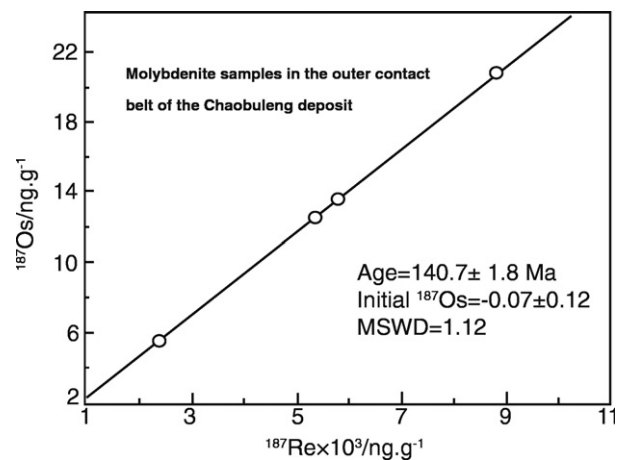


Fig. 12. Re–Os isochron age of molybdenites from the outer contact belt of Chaobuleng iron polymetallic deposit. The ISOPLOT software of Ludwig (2004) was used to calculate the isochron age, decay constant: $\lambda (^{187}\text{Re}) = 1.666 \times 10^{-11}/\text{year}$ (Smoliar et al., 1996), uncertainties are absolute at 2σ with error of 1.01% at 95% confidence level. The data from Nie et al. (2007).

saturation temperature estimate using Eq. (1) above for the syenogranite porphyry is ~ 855 °C. The calculated estimates for the enclave bearing porphyritic syenogranite and the coarse-grained porphyritic syenogranite are ~ 828 °C and ~ 800 °C, respectively. These T_{Zr} values provide a minimum estimate for magma temperature at the source during zircon formation and indicate that these A-type granitoids all formed at relatively high temperatures. The syenogranite porphyry was the hottest. The mafic enclaves fall outside of the original calibration range of the zircon saturation thermometer, and thus their calculated apparent zircon saturation temperatures may have no geological significance (Hanchar and Watson, 2005; Boehnke et al., 2013).

The estimated formation temperature, pressure, and emplacement depth of the Chaobuleng pluton are 720–770 °C, 0.5–1.0 kbar and 1.7–3.5 km, respectively, as calculated on a Q–Ab–Or system phase diagram (data from Nie et al., 2007 and Wang et al., 2014) and from mineral geobarometry (Fig. 16). In a biotite Ti–Mg[#] diagram (Henry et al., 2005) (Fig. 17), the estimated temperatures of biotite range from 700 to 750 °C which is comparable to the low eutectic-point temperatures (720–770 °C) calculated from the aforementioned Q–Ab–Or system phase diagram. Grains of biotite, quartz, and feldspar appear to have crystallized simultaneously (Fig. 8). All of the above characteristic indicate that the biotite grains were produced by late-stage crystallization differentiation.

5.2.2. Petrogenesis and tectonic implications

If the petrogenesis of the Chaobuleng pluton involves fractional crystallization, then all three plutonic units would have been derived from the same source region, undergoing magmatic differentiation from a common parent magma. However, our geochemical and U–Pb zircon data show the SiO_2 contents increase from the coarse-grained porphyritic syenogranite (133.9–135.98 Ma) to enclave bearing porphyritic syenogranite (137.4–138.6 Ma), and are highest for the syenogranite porphyry (138.1–140.6 Ma). In addition, the granitic felsic component endmembers in the enclave bearing porphyritic syenogranite show strong mixing with mafic dioritic magma (Fig. 18). The embayed plagioclase feldspar inclusions show signs of strong mafic enrichment when plotted on the feldspar mineral Ab–Or–An diagram (Fig. 13A): plagioclase cores with An 30 mixed with felsic magma (plagioclase An 5–10) resulting in hybrid plagioclase grains with An 10–20.

We favor this magma mixing model because it could produce the mixing curves observed in both the isotopic correlation diagrams and isotopic ratios versus various elements (e.g., MgO, SiO_2) plots (Fig. 10). Furthermore, there are strong field-based indications for magmatic

mixing, including mafic microgranular enclaves, porphyritic texture, and disequilibrium textures (Fig. 8). The melt inclusions show considerably more compositional heterogeneity in trace element ratios than the matrix glasses. These ratios (e.g., La/Yb) are not affected by fractional crystallization or by post-entrapment crystallization, and therefore reflect compositional differences inherited from primary melts. This higher degree of compositional variability in melt inclusions has been previously observed and discussed, and is thought to be related to the mixing process. Heterogeneous melts produced in the mantle are gradually mixed together, eventually producing relatively homogeneous carrier liquids in a relatively shallow plumbing system (Kent and Elliott, 2002). The composition of the matrix glasses is within the ranges

defined by the melt inclusions, which is consistent with being genetically related via mixing. In addition, the biotite $W(\text{Feo})/W(\text{MgO} + \text{MgO}) - W(\text{MgO})$ diagram can distinguish the material source of the granitoids (Zhou, 1986). Samples from the Chaobuleng pluton plotted into the field of the crust-mantle mixing (Fig. 19), and we interpret this to represent the magma source environment.

Most granitoid samples from the Chaobuleng pluton plotted in the field of A-type granites (Fig. 11), which are generally associated with an extensional setting regardless of the origin of the magma source (e.g., Whalen et al., 1987; Eby, 1990, 1992; Turner et al., 1992). Mesozoic ore deposits in eastern China are related to lithospheric thinning, caused by the upwelling of the asthenosphere during continental extension

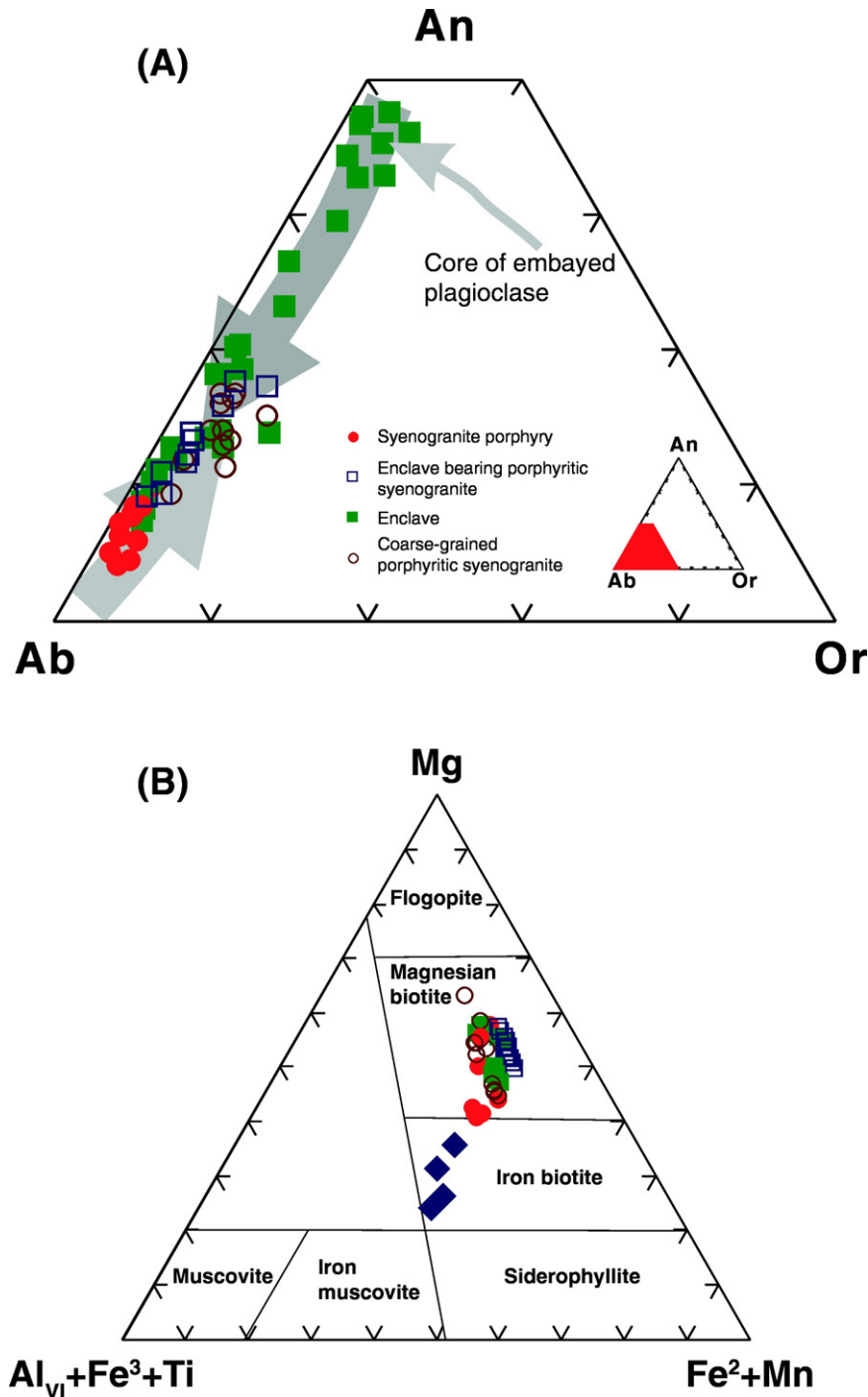


Fig. 13. (A) An-Ab-Or (anorthite-albite-orthoclase ternary) diagram for the feldspars of the Chaobuleng granitoids. Base map modified after Evans and Moore (1968). (B) Composition classification diagram of the biotite mineral from the Chaobuleng granitoids. Base map modified after Sun and Yu (1989).

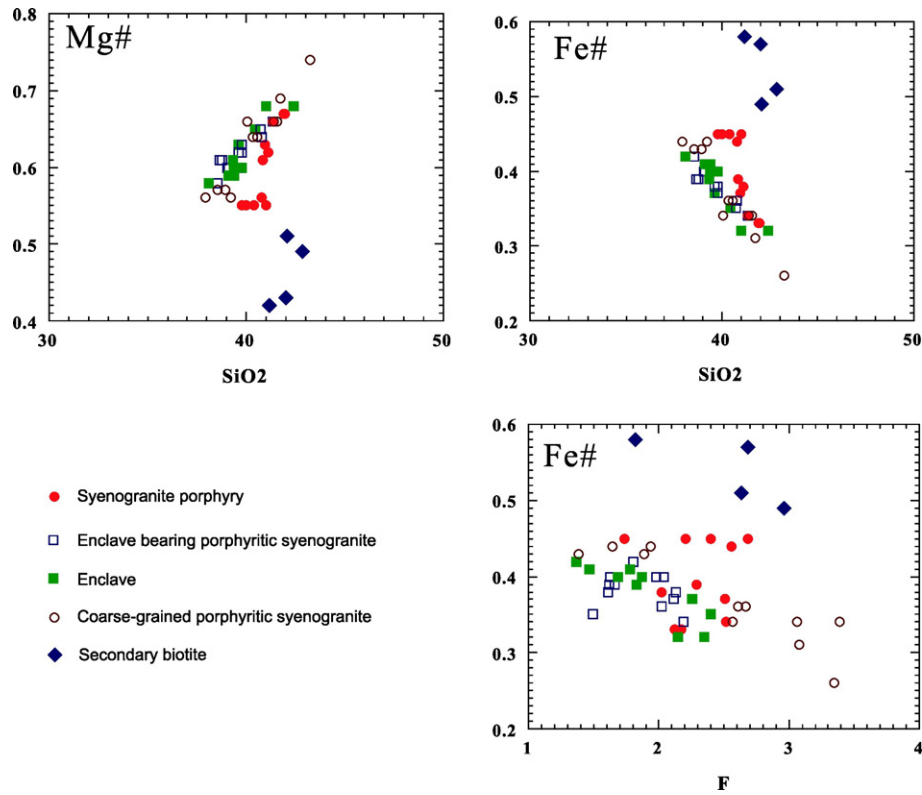


Fig. 14. Chemical composition diagram of biotite mineral from the Chaobuleng granitoids. Base map modified after Stone (2000).

(Chen et al., 2009; Wu et al., 2014, 2015). The dynamic setting may be linked to the subduction of the Izanagi plate beneath the Eurasian plate during the Early Cretaceous (Isozaki, 1997; Mao et al., 2005; Wu et al., 2014). Other metallogenic belts in the CAO (e.g. the Xilamulun Mo-Cu metallogenic belt, Fig. 1) were also affected by Izanagi plate subduction (Zhang et al., 2009; Zeng et al., 2010). Subduction-related ore deposits in these belts during the Late Jurassic to Early Cretaceous period involve a similar tectonic setting of lithospheric thinning and

magmatic underplating (Zhang et al., 2009; Wu et al., 2014, 2015). Magmatic fluids that originated from granitic magmas or the deep magma chambers during the Mesozoic era supplied significant amounts of sulfur and other base metals to form large-scale hydrothermal deposits in northeastern China. Izanagi plate subduction also triggered intensive magmatism and mineralization in the Great Xing'an Range (Wu et al., 2005a, 2005b; Wu et al., 2014, 2015). Intermediate-mafic magma underplating beneath relatively young continental crust would have

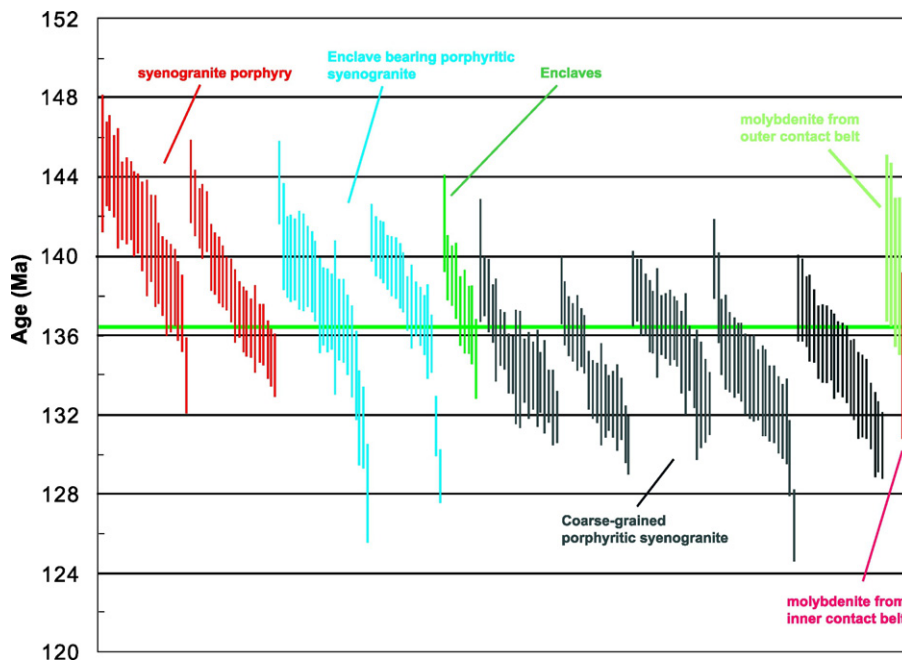


Fig. 15. Distribution diagram of the Zircon $^{207}\text{Pb}/^{235}\text{U}$ - $^{206}\text{Pb}/^{238}\text{U}$ concordia ages from the Chaobuleng granitoids and the Re-Os isochron age of molybdenites from the Chaobuleng iron polymetallic deposit. The data from Nie et al. (2007) and this study.

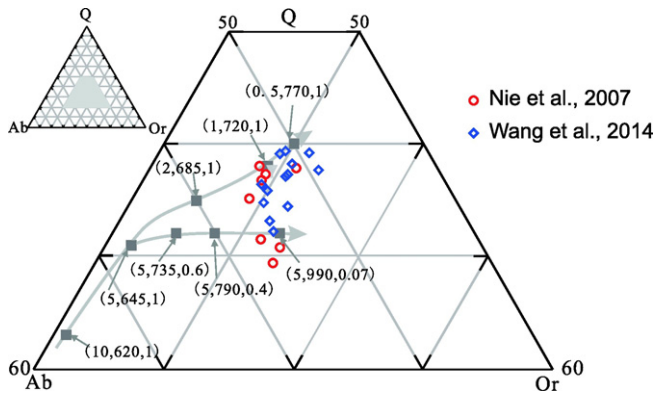


Fig. 16. Normal Q-Ab-Or mineral phase diagram from the samples of Chaobuleng pluton. Base map modified after Johannes and Holtz (1996) and Becker et al. (1998). Composition of minima and eutectics in Q-Ab-Or granitic melt as a function of pressure, temperature and water activity. For $P = 1 \times 10^8$ Pa, $T = 720$ °C, $a_{H_2O} = 1$, labeled as (1, 720, 1) in this figure, melt minima is $Q_{38}Ab_{33}Or_{29}$ and $w(H_2O)$ is 3.7%. The data from Nie et al. (2007) and Wang et al. (2014).

provided the necessary heat to result in partial melting near the crust-mantle boundary. In turn, this process could have driven crust-mantle magma mixing.

5.3. Mineralization process and styles

The Chaobuleng iron polymetallic deposit consists of calc-silicate minerals (e.g., garnet, epidote), iron oxide minerals (i.e., magnetite is the dominant ore mineral, usually accompanied by galena, and cassiterite), sulfide minerals (e.g., molybdenite, bismuthinite, chalcocopyrite, pyrite, sphalerite, and gellenite), other silicate minerals (e.g., biotite), calcite, and F-bearing minerals (e.g., actinolite). The above mineralization features and mineral assemblages of the Chaobuleng iron polymetallic deposit are similar to most skarn-type mineral deposits (Einaudi et al., 1981; Zhao et al., 1990; Meinert, 1992; Meinert et al., 2005).

The minerals, colors, structural zoning observed in the skarns in Chaobuleng polymetallic deposit record the physical and chemical conditions of the magmatic hydrothermal fluids. The water/rock ratio is higher near the Chaobuleng pluton which resulted in massive skarns, whereas metasomatic skarns are developed farther from the Chaobuleng pluton. The occurrence of wollastonite skarn at the contact between the skarns and limestone suggests a relatively high carbon dioxide fugacity of the fluids, according to the T- f_{CO_2} phase diagram of the skarn deposit (Meinert, 1992). Locally the occurrence of the hematite indicates a relatively high oxygen fugacity. However, the rock type (i.e., red garnet skarn, yellow garnet skarn, and green pyroxene in spatial order from the pluton to the wall rock) indicates that oxygen fugacity gradually decreases away from the pluton, which suggests that the intrusion triggered skarn development (Meinert, 1992). The retrograde alteration minerals in the Chaobuleng deposit are mainly epidote, hornblende, biotite, chlorite, iron oxides, polymetallic sulfides, quartz, fluorite, and calcite, which overprint the prograde alteration skarns. The mineral assemblage depends on fluid composition, oxygen fugacity, and sulfur fugacity. The mineral assemblage of magnetite and specularite during the iron oxide stage show the relatively high oxygen fugacity, whereas the occurrence of the sulfide minerals indicates the relatively high sulfide fugacity during the polymetallic sulfur stage. These features are traditionally considered as part of the magmatic hydrothermal skarn iron polymetallic deposit (Zhao, et al., 1990).

We identify four stages of hydrothermal evolution from Chaobuleng iron polymetallic deposit. The decrepitation temperatures (Table 3) of (1) the garnet grains range from 515 to 525 °C during the high temperatures stage, (2) the magnetite and maghemite grains range from 450 to

480 °C, (3) the sulfide minerals range from 380 to 480 °C, and (4) the molybdenite collected from the molybdenite-pyrite vein range from 200 to 300 °C. The molybdenite is interpreted to have been produced during the late stage of mineralization.

The formation of high-grade iron ores involves iron precipitation from hydrothermal fluids with high iron-concentration. Previous studies considered two principal sources of the iron: (1) exsolution of Fe-rich magmatic fluids from the melt at depth, and (2) leaching from the wall-rock sedimentary rocks and/or solidified mafic intrusion at a relatively shallow level (Zhao et al., 1986). The country rocks in the Chaobuleng orefield consist mainly of the Ordovician carbonates which have relatively high iron contents. The physical and chemical conditions of the Chaobuleng pluton are described in the aforementioned Q-Ab-Or phase diagram (Nie et al., 2007; Wang et al., 2014) (Fig. 16). Therefore, the dominant source of iron may be the exsolution of Fe-rich magmatic fluids and leaching from the solidified mafic intrusion at a relatively shallow level. Furthermore, the Chaobuleng iron polymetallic deposit was formed as a hypabyssal, high temperature, and proximal skarn type deposit. The Chaobuleng Fe skarn deposit is genetically related to the Fe-enriched magmatic hydrothermal fluid, which exsolved from the primary magma of the Chaobuleng complex pluton. The primary magma was derived from a source with high oxygen fugacity, which favors the metallogensis of skarn iron deposit. The Fe enrichment in ore-forming fluid experienced a two-stage process: original partitioning of Fe into the magmatic hydrothermal fluid and later Fe-leaching process.

5.4. Magma-hydrothermal fluid transition

Fluorite appears in every stage of mineralization in Chaobuleng iron polymetallic deposit. Additionally, the crystallization of silicate minerals, particularly iron-poor minerals, further elevates the iron concentration in the residual magma. The occurrence of F-rich minerals such as fluorite and biotite (i.e., F contents in the biotite grain are 1.5–3.6%) in the Chaobuleng ore-forming fluid suggests that the melt and/or fluids were F-bearing. Since the solubility of iron is strongly enhanced by the presence of F in hydrothermal fluids (Webster and Holloway, 1990), iron tends to concentrate into the fluids and form Fe-rich magmatic hydrothermal fluids during the exsolution of the magmatic fluids. Fluorine decreases the liquidus and especially the solidus temperature of melts (Chang and Meinert, 2004, 2008). Manning (1981) showed that F can decrease the solidus temperature of granitic melts to below 550 °C.

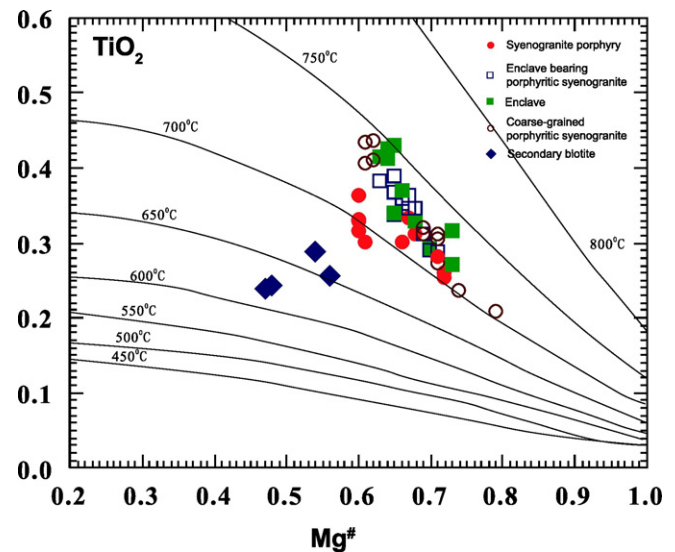


Fig. 17. Crystallization temperature diagram of biotite from the Chaobuleng granitoids. Base map modified after Henry et al. (2005).

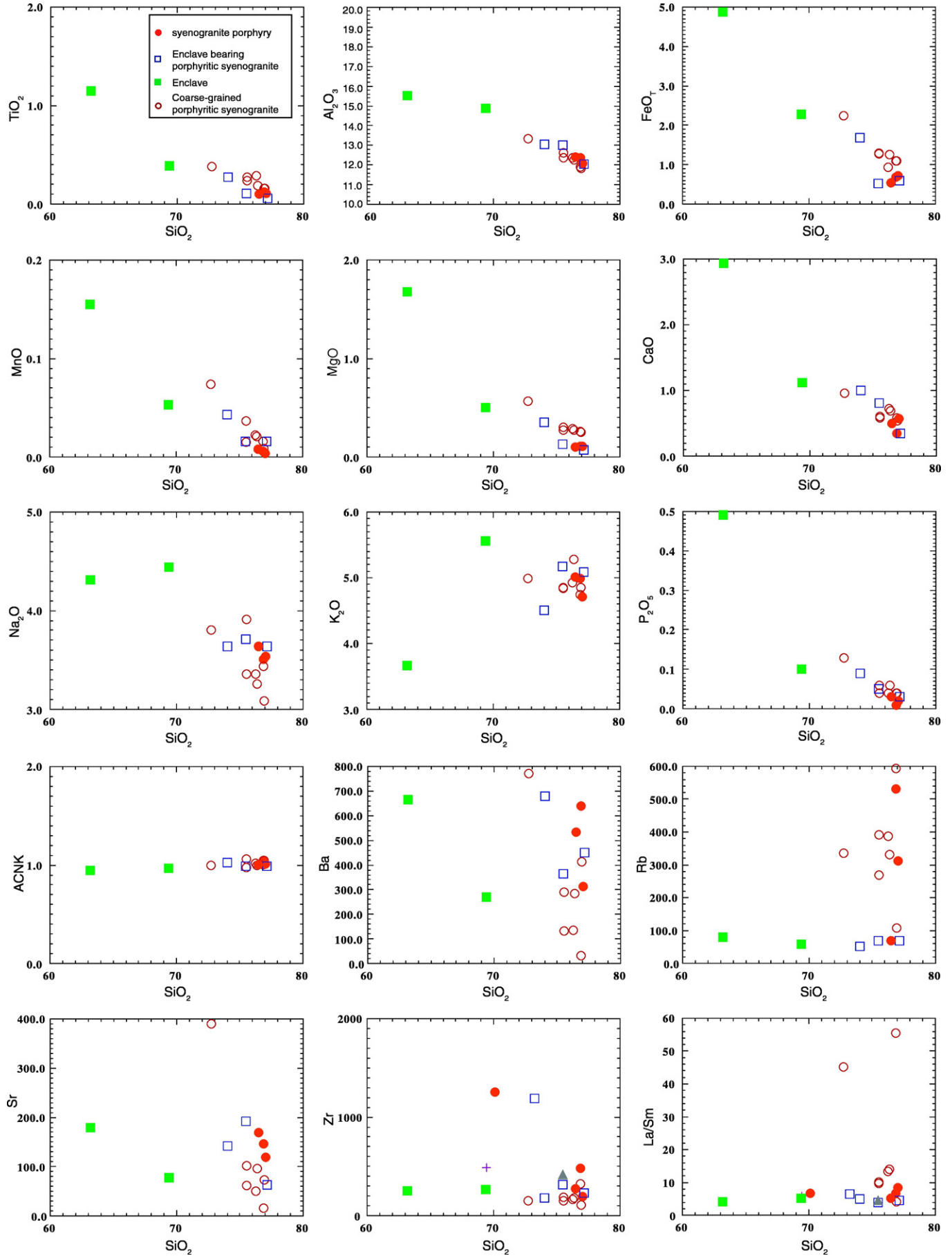


Fig. 18. Harker diagrams of the Chaobuleng granitoids showing content variation of major elements.

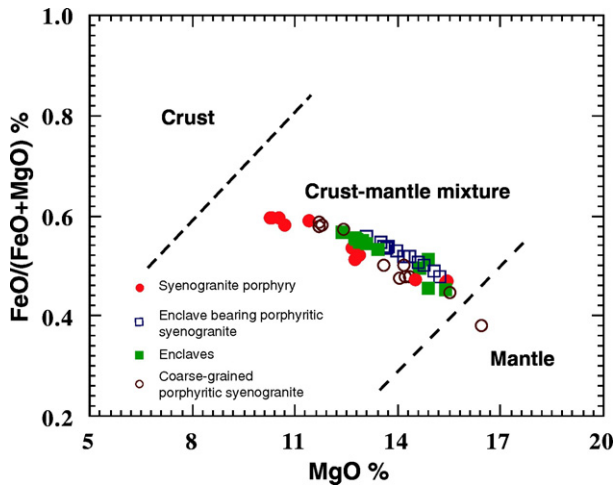


Fig. 19. $W(\Sigma\text{FeO})/W(\Sigma\text{FeO} + \text{MgO})-W(\text{MgO})$ diagram of the biotite diagram from the Chaobuleng granitoids. Base map modified after Zhou (1986).

It is commonly accepted that the magmatic-hydrothermal transition plays a critical role in the formation of hydrothermal ore deposits with respect to both physical and chemical process (e.g., Hedenquist and Lowenstern, 1994; Chang and Meinert, 2004). Information about this transition is recorded in the texture, mineralogy, and melt/fluid inclusions of some igneous rocks. In this study, we document extremely embayed quartz phenocrysts, an igneous texture that formed during the magmatic-hydrothermal transition. Embayed quartz phenocrysts are commonly present in many volcanic rocks and some granitic intrusive rocks. The hypotheses for quartz embayments can be grouped into two categories: melt resorption or special quartz growth (Chang and Meinert, 2004). More specifically, the origin of embayed quartz has been interpreted to result from: (1) resorption of quartz by the melt due to ascending and decompression (e.g. Nekvasil, 1991; Eklund and Shebanov, 1999); (2) resorption of quartz due to

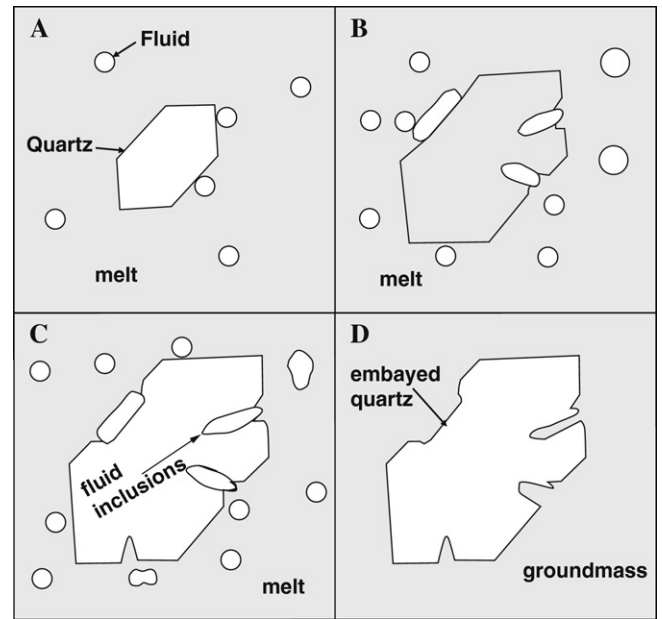


Fig. 20. Model for the development of embayed textures in quartz phenocrysts; see text for detailed explanation.

magma mixing (e.g. Sakuyama, 1979, 1981; Burt et al., 1996; Kontak and Clark, 1997; Kuscus and Floyd, 2001); (3) resorption of quartz due to decreased F activity in the melt after some F partitions into the magmatic aqueous fluid (Webster, 1990); (4) rapid growth due to undercooling, which results in skeletal textures (e.g. Swanson and Fenn, 1986; Candela, 1997); and (5) cellular growth (McCutcheon and Robinson, 1988; McCutcheon, 1990).

The observed embayed quartz from the Chaobuleng pluton has the following characteristics. Quartz is most dominantly embayed in the fine-grained groundmass and less so near the margin of the quartz

Table 3
Decrepiation temperature of opaque mineral, garnet and quartz in the Chaobuleng iron polymetallic deposit.

Mineral	Weight (mg)	Decrepiation temperature °C				Decrepiation total	Feature of ore
		I	II	III	IV		
Pyrrhotite	30			392	287	3129/100–450 °C	Polymetallic sulfide-arsenopyrite ore, containing a small amount of early stage magnetite mineralization
Magnetite	30		476	376	255	4850/100–650 °C	Garnet skarn, magnetite with a small amount of superimposed mineralization, superposition of sphalerite mineralization
Magnetite	30		454	330	245	675/100–500 °C	Magnetite-arsenopyrite ore, containing chalcopyrite, pyrite and fluorite in late stage
Magnetite	30		410			392/100–650 °C	Chalcopyrite-pyrite ore, containing magnetite mineralization in early stage
Magnetite	30		485	318		982/100–650 °C	Magnetite ore, containing chalcopyrite, sphalerite, and fluorite in late stage
Magnetite	30	525	470	324	243	752/100–650 °C	Magnetite ore, containing chalcopyrite and sphalerite in late stage
Magnetite	30		482	382	309	3574/100–650 °C	Magnetite ore
Arsenopyrite	30		313	267		560/100–400 °C	Arsenopyrite-magnetite ore
Pyrite	30		315			362/100–390 °C	Magnetite-arsenopyrite ore, containing chalcopyrite in late stage
Pyrite	30		322			406/100–390 °C	Chalcopyrite-pyrite ore, containing magnetite mineralization in early stage
Chalcopyrite	30		282			3200/100–390 °C	Magnetite ore, containing chalcopyrite in late stage
Chalcopyrite	30		294			2989/100–390 °C	Chalcopyrite-pyrite ore, containing magnetite mineralization in early stage
Molybdenite	30			250		166/100–390 °C	Fluorite-molybdenite-pyrite vein in granite
Specularite	30		456	380	220	8315/100–350 °C	Magnetite-specularite, containing garnet in late stage
Sphalerite	30			340	242	2713/100–390 °C	Garnet skarn, magnetite with a small amount of superimposed mineralization and superposition of sphalerite mineralization
Sphalerite	30			306	215	3750/100–390 °C	Garnet skarn, containing sphalerite mineralization in late stage
Sphalerite	30			299	222	3218/100–390 °C	Sphalerite ore, containing magnetite mineralization in early stage
Garnet	30	516	407	306	260	2443/100–500 °C	Magnetite-specularite, containing garnet in late stage
Garnet	30		403			160/100–500 °C	Garnet skarn, containing sphalerite mineralization in late stage
Garnet	30	525	426			110/100–500 °C	Garnet skarn, containing sphalerite mineralization in late stage
Quartz	20		466	390	294	2652/100–500 °C	Chalcopyrite-pyrite ore, containing magnetite mineralization in early stage
Quartz	20		490	405	330	6661/100–500 °C	Granite in margin of pluton
Quartz	20		488	392	198	6338/100–500 °C	Granite in margin of pluton
Fluorite	10			338	267	10,934/100–500 °C	Magnetite-arsenopyrite ore, containing chalcopyrite, pyrite and fluorite in late stage
Fluorite	10			335	262	3047/100–500 °C	Magnetite ore, containing chalcopyrite, pyrite and a large amount of fluorite in late stage

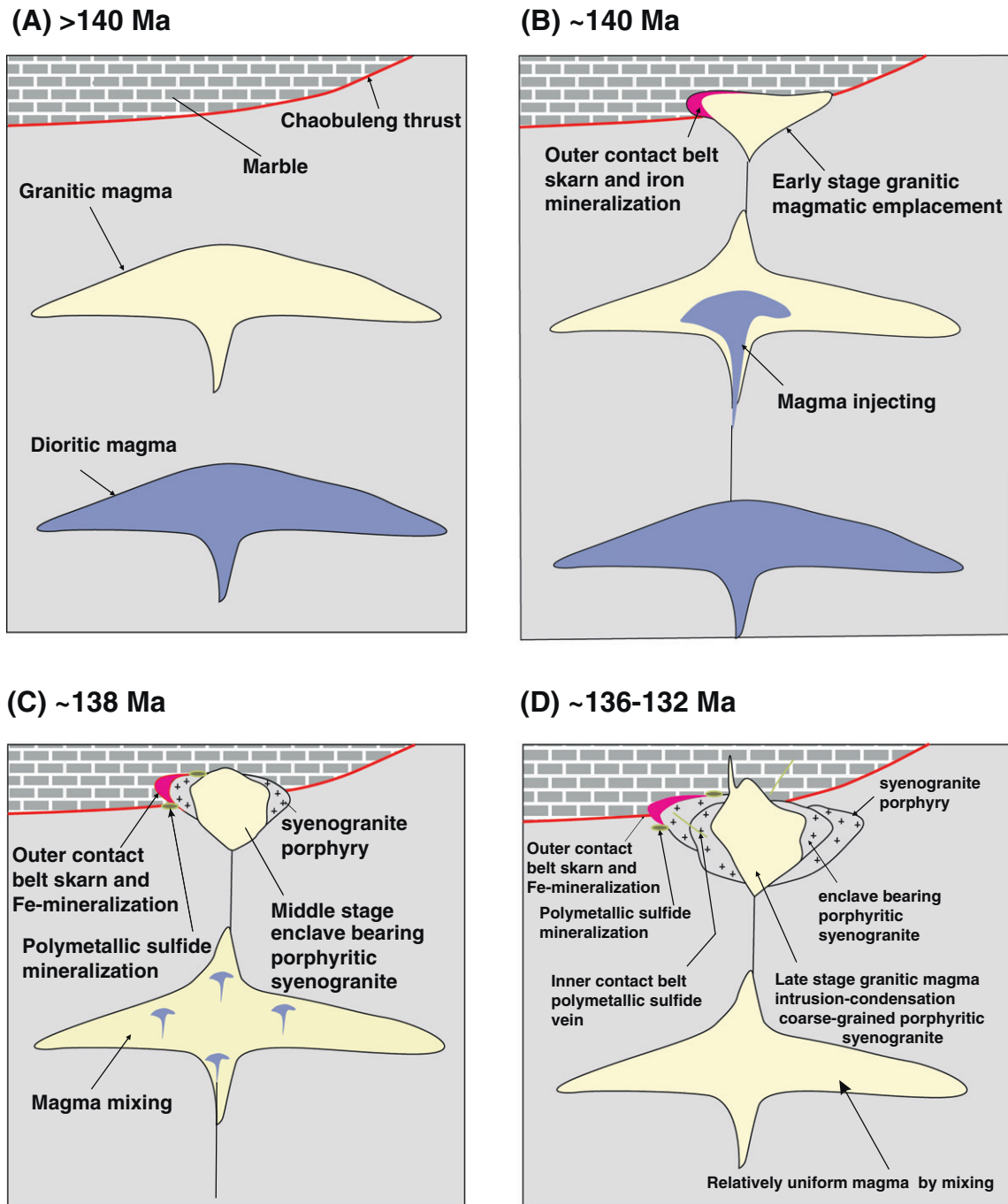


Fig. 21. (A–D) Magmatic mineralization pattern model of the Chaobuleng iron polymetallic deposit. See text for details.

phenocrysts, which indicates the low pressures (0.5–1 kbar) near the quartz-plagioclase-alkali feldspar-biotite eutectic point. There is high F content observed in biotite, and with high-F activity in the fluid, the dissolution of the quartz may occur faster, facilitating the formation of extensive, deep, and sinuous embayments. Also, as previously discussed, fluorite appears in each stages of mineralization as an accessory mineral.

The three coexisting phase equilibrium model for granitoid–magmatic hydrothermal fluid–quartz of Chang and Meinert (2004, 2008) may best explain the quartz resorption texture in the Chaobuleng pluton. Due to loss of volatiles, residual melt was quickly quenched and crystallized into fine-grained matrix (Fig. 20). The formation of embayed quartz textures is proposed as follows. (1) Quartz crystallizes

from the phenocryst containing magma. Initially, the amount of hydrothermal fluid is small and the fluid nucleates as bubbles within the magma (Fig. 20A). At this stage, both the magma and hydrothermal fluid are rich in F. (2) Where the fluid bubbles rich in F adhere to quartz crystals, the bubbles corrode into the quartz phenocrysts, forming rounded, elongate, and sinuous embayments (Fig. 20B). The high F activity further enhances the corrosion process allowing very deep embayment to form in the quartz phenocrysts. If the magma does not erupt, crystallization of minerals will again cause the melt to become quartz saturated. The new quartz growth forms the curving outer/later bands (Fig. 20C). (3) When sufficient hydrothermal fluid accumulates to hydro-fracture the outer crust of the magma body (Cashman and Mangan, 1994; Shinohara and Hedenquist, 1997), the melt

quenches and the remaining melt crystallizes in the groundmass and embayments (Fig. 20D).

Based on the data outlined in this study, we propose the following model to explain the relationship between the magma and the mineralization of the Chaobuleng iron polymetallic deposit (Fig. 21). Prior to 140 Ma, lower crust/upper mantle underplating of hot mafic magma led to the melting of the lower crustal rocks and the formation of the granitic magma ($\text{SiO}_2 \sim 77\%$) rich in F (Fig. 21A). At ~ 140 Ma, mafic magma melts into the granitic magma and triggered the upwelling of the granitic magma from the felsic magma chamber, leading to the emplacement of the syenogranite porphyry (138.1–140.6 Ma) near the Chaobuleng thrust (Fig. 2B). Stress changes caused by fault motion may have led to the exsolution of F-rich fluid from limestone or marble during the early stages of prograde alteration (skarn or hornfels) in the outer contact zone and iron oxide mineralization. The polymetallic sulfide mineralization during this stage is related to the retrograde alteration. The syenogranitic porphyry magma cooled rapidly and formed a fine-grained groundmass. As the result of weak magma mixing, the melt remained relatively felsic ($\text{SiO}_2 \sim 77\%$) (Fig. 21B). Next, the enclave bearing porphyritic syenogranite (137.4–138.6 Ma) formed via mixing of the intermediate-mafic magma and the felsic F-rich magma. The development of disequilibrium textures is related to this strong magma-mixing event. Polymetallic sulfide mineralization of the outer contact belt also developed during this time (Fig. 21C). At ~ 136 – 132 Ma, mixing between the intermediate-mafic magma and the felsic F-rich magma led to the generation of a relatively uniform melt (SiO_2 70–75%) that formed the coarse-grained porphyritic syenogranite (133.9–135.98 Ma). Residual plagioclase inclusions ($An = 30$) also developed within the phenocrysts. At this stage, F-rich fluid forms the polymetallic sulfide mineralization, especially in the inner contact belt, as polymetallic sulfide veins (Fig. 21D).

6. Conclusions

Mineralization and alteration of the Chaobuleng iron polymetallic deposit occurred along the contact zone between pluton and wall rock. In the wall rock, prograde skarns with a garnet + pyroxene + wollastonite \pm calcite assemblage or hornfels with a hornblende + biotite + plagioclase + quartz assemblage were produced by metasomatic alteration of marble or mud-sandstone. Along the margins of the pluton, veins with a potassium feldspar + biotite \pm garnet assemblage developed during metasomatic alteration of the granitoid. Retrograde epidote also developed. The sulfide vein formed a chlorite halo that was superimposed by later retrograde alteration. Finally, hydrothermal activity ended with extensive argillization. Our field observations, inferred paragenesis, and observed P - T conditions suggest that the Chaobuleng Fe polymetallic deposit formed as a shallow (1.7–3.5 km) proximal skarn deposit.

The Mesozoic ore-forming Chaobuleng pluton can be divided into three units: (1) a 138.1–140.6 Ma syenogranite porphyry, (2) a 137.4–138.6 Ma enclave bearing porphyritic syenogranite, and (3) a 133.9–135.98 Ma coarse-grained porphyritic syenogranite. The observed spectrum of individual U-Pb zircon ages indicate that magmatic activity lasted for nearly ~ 17 million years. Our Re-Os molybdenite ages show that mineralized hydrothermal activity occurred over a duration of ~ 9 million years. These age constraints suggest that the Chaobuleng deposit resulted from protracted activities of a large magma-hydrothermal system. However, the major mineralization stage of Chaobuleng deposit (iron oxide stage) occurred during the early stage of magmatism, consistent with the emplacement time of the syenogranite porphyry (~ 139 Ma).

The Chaobuleng pluton formed in a post-orogenic extensional setting. The A-type granites display high Zr saturation temperatures of 800–900 °C. The estimated eutectic temperature was as low as 720–770 °C with pressures at 0.5–1 kbar. The chemical composition of biotite shows that the Chaobuleng magma was enriched in F-component (1.5–

3.5%). However, the mixing of granitic magma and partially mafic magma can satisfactorily explain the petrogenesis of the Chaobuleng pluton. In addition, the observed strong embayment texture in quartz may be best explained by a three coexisting-phase-equilibrium model, where the loss of volatiles results in the rapid quenching of residual melt that crystallized into a fine-grained groundmass.

Supplementary data to this article can be found online at <http://dx.doi.org/10.1016/j.gr.2017.02.006>.

Acknowledgments

This work was supported by the Inner Mongolia Mapping Programs (Project number: 1212010811001, 1212011120700, DD20160045, 1212010510506) awarded to Zhiguang Zhou and administered by the Institute of Geological Survey, China University of Geosciences (Beijing). We thank Associate Editor Franco Pirajno and two anonymous reviewers for their very constructive reviews that led to significant improvement of the original manuscript.

References

- Andersen, T., 2002. Correction of common lead in U–Pb analyses that do not report ^{204}Pb . *Chem. Geol.* 192, 59–79.
- Armstrong, J.T., 1995. Citzaf-a package of correction programs for the quantitative electron microbeam X-ray-analysis of thick polished materials, thin-films, and particles. *Microbeam Anal.* 4 (3), 177–200.
- Batchelor, R.A., Bowden, P., 1985. Petrogenetic interpretation of granitoid rock series using multicationic parameters. *Chem. Geol.* 48 (1–4), 43–55.
- Black, L.P., Kamo, S.L., Allen, C.M., Aleinikoff, J.N., Davis, D.W., Korsch, R.J., Foudoulis, C., 2003. TEMORA 1: a new zircon standard for Phanerozoic U–Pb geochronology. *Chem. Geol.* 200 (1), 155–170.
- Becker, A., Holtz, F., Johannes, W., 1998. Liquidus temperatures and phase compositions in the system Qz–Ab–Or at 5 kbar and very low water activities. *Contrib. Mineral. Petrol.* 130, 213–224.
- Boehnke, P., Watson, E.B., Trail, D., Harrison, T.M., Schmitt, A.K., 2013. Zircon saturation revisited. *Chem. Geol.* 351, 324–334.
- Boynnton, W.V., 1984. Cosmochemistry of the rare earth elements: Meteorite studies. In: Henderson, P. (Ed.), *Rare Earth Element Geochemistry*: Amsterdam, Netherlands, Elsevier. pp. 63–114. <http://dx.doi.org/10.1016/B978-0-444-42148-7.50008-3>.
- Burt, R.M., Cole, J.W., Vroon, P.Z., 1996. Volcanic geology and geochemistry of Motuhora (Whale Island), Bay of Plenty, New Zealand. *N. Z. J. Geol. Geophys.* 39, 565–580.
- Candela, P.A., 1997. A review of shallow, ore-related granites: textures, volatiles, and ore metals. *J. Petrol.* 38, 1619–1633.
- Cashman, K.V., Mangan, M.T., 1994. Physical aspects of magmatic degassing II. Constrains on vesiculation processes from textural studies of eruptive products. *Rev. Mineral. Geochem.* 30, 457–478.
- Chang, Z.S., Meinert, L.D., 2004. The magmatic–hydrothermal transition—evidence from quartz phenocryst textures and endoskarn abundance in Cu–Zn skarns at the Empire Mine, Idaho, USA. *Chem. Geol.* 21, 149–171.
- Chang, Z.S., Meinert, L.D., 2008. The empire Cu–Zn mine, Idaho: exploration implications of unusual skarn features related to high fluorine activity. *Econ. Geol.* 103, 909–938.
- Chen, Y.J., Chen, H.Y., Zaw, K., Pirajno, F., Zhang, Z.J., 2007. Geodynamic settings and tectonic model of skarn gold deposits in China: an overview. *Ore Geol. Rev.* 31, 139–169.
- Chen, Y.J., Zhai, M.G., Jiang, S.Y., 2009. Significant achievements and open issues in study of orogenesis and metallogenesis surrounding the North China continent. *Acta Petrol. Sin.* 25, 2695–2726 (in Chinese with English abstract).
- Chen, Z.G., Zhang, L.C., Wan, B., Wu, H.Y., Clevon, N., 2011. Geochronology and geochemistry of the Wunuetushan porphyry Cu–Mo deposit in NE China, and their geological significance. *Ore Geol. Rev.* 43, 92–105.
- Dai, J.G., Wang, C.S., Hourigan, J., Santosh, M., 2013. Multi-stage tectono-magmatic events of the eastern Kunlun range, northern Tibet: insights from U–Pb geochronology and (U–Th)/He thermochronology. *Tectonophysics* 599, 97–106.
- De Jong, K., Xiao, W.J., Windley, B.F., Masago, H., Lo, C.H., 2006. Ordovician 40Ar/39Ar phengite ages from the blue schist-facies Ondor Sum subduction-accretion complex (Inner Mongolia) and implications for the early Paleozoic history of continental blocks in China and adjacent areas. *Am. J. Sci.* 306 (12), 799–845.
- Dill, H.G., 2010. The “chessboard” classification scheme of mineral deposits: mineralogy and geology from aluminum to zirconium. *Earth-Sci. Rev.* 100, 1–420.
- Eby, G.N., 1990. The A-type granitoids: a review of their occurrence and chemical characteristics and speculations on their petrogenesis. *Lithos* 26, 115–134.
- Eby, G.N., 1992. Chemical subdivision of the A-type granitoids: petrogenetic and tectonic implications. *Geology* 20, 641–644.
- Einvaldi, M.T., Meinert, L.D., Newberry, R.J., 1981. Skarn deposits. *Econ. Geol.* 75, 317–391.
- Eklund, O., Shebanov, A.D., 1999. The origin of rapakivi texture by sub-isothermal decompression. *Precambrian Res.* 95, 129–146.
- Evans, B.W., Moore, J.G., 1968. Mineralogy as a function of depth in the prehistoric Makaopuhi tholeiitic lava lake, Hawaii. *Contrib. Mineral. Petrol.* 17 (2), 85–115.
- Frost, C.D., Frost, B.R., 1997. Reduced rapakivi-type granites: the tholeiite connection. *Geology* 25 (7), 647–650.

- Gao, S., Rudnick, R.L., Xu, W.L., Yuan, H.L., Liu, Y.S., Walker, R.J., Puchtel, I.S., Liu, X.M., Huang, H., Wang, X.R., Yang, J., 2008. Recycling deep cratonic lithosphere and generation of intraplate magmatism in the North China craton. *Earth Planet Sci. Lett.* 270, 41–53.
- Guo, F., Fan, W.M., Gao, X.F., Li, C.W., Miao, L.C., Zhao, L., Li, H.X., 2010. Sr–Nd–Pb isotope mapping of Mesozoic igneous rocks in NE China: constraints on tectonic framework and Phanerozoic crustal growth. *Lithos* 120, 563–578.
- Halliday, A.N., 1980. The timing of early and main stage ore mineralization in southwest Cornwall. *Econ. Geol.* 75, 752–759.
- Hanchar, J.M., Watson, E.B., 2005. Zircon saturation thermometry. *Rev. Mineral. Geochem.* 53 (1), 89–112.
- Harley, S.L., Kelly, N.M., Möller, A., 2007. Zircon behaviour and the thermal histories of mountain chains. *Elements* 3 (1), 25–30.
- Hedenquist, J.W., Lowenstern, J.B., 1994. The role of magmas in the formation of hydrothermal ore deposits. *Nature* 370 (6490), 519–527.
- Henry, D.J., Guidotti, C.V., Thomson, J.A., 2005. The Ti–saturation surface for low-to-medium pressure metapelitic biotites: implications for geothermometry and Ti-substitution mechanisms. *Am. Mineral.* 90 (2–3), 316–328.
- Hu, R.Z., Zhou, M.F., 2012. Multiple Mesozoic mineralization events in South China—an introduction to the thematic issue. *Mineral. Deposita* 47, 579–588.
- Isizaki, Y., 1997. Jurassic accretion tectonics of Japan: the island arc. 6 pp. 25–51.
- Jahn, B.M., Wu, F.Y., Chen, B., 2000. Massive granitoids generation in central Asia: Nd isotopic evidence and implication for continental growth in the Phanerozoic. *Episodes* 23, 82–92.
- Jahn, B.-M., Windley, B., Natal'in, B., Dobretsov, N., 2004a. Phanerozoic continental growth in Central Asia. *J. Asian Earth Sci.* 23, 599–603.
- Jahn, B.-M., Capdevila, R., Liu, D.Y., Vernon, A., Badarch, G., 2004b. Sources of Phanerozoic granitoids in the transect Bayanhongor–Ulaan Baatar, Mongolia: geochemical and Nd isotopic evidence, and implications for Phanerozoic crustal growth. *J. Asian Earth Sci.* 23, 629–653.
- Johannes, W., Holtz, F., 1996. *Petrogenesis and Experimental Petrology of Granitic Rocks*. Springer-Verlag, Berlin, pp. 1–135.
- Kent, A.J.R., Elliott, T.R., 2002. Melt inclusions from Marianas arc lavas: implications for the composition and formation of island arc magmas. *Chem. Geol.* 183 (1), 263–286.
- Kontak, D.J., Clark, A.H., 1997. The Minastira paraluminous granite, Puno, southeastern Peru: a quenched, hypabyssal intrusion recording magma commingling and mixing. *Min. Mag.* 61, 743–764.
- Kröner, A., Hegner, E., Lehmann, B., Heinhorst, J., Wingate, M.T.D., Liu, D.Y., Ermelov, P., 2008. Palaeozoic arc magmatism in the central Asian Orogenic Belt of Kazakhstan: SHRIMP zircon ages and whole-rock Nd isotopic systematics. *J. Asian Earth Sci.* 32, 118–130.
- Kröner, A., Lehmann, J., Schulmann, K., Demoux, A., Lexa, O., Tomurhuu, D., Stipská, P., Liu, D.Y., Wingate, M.T.D., 2010. Lithostratigraphic and geochronological constraints on the evolution of the Central Asian Orogenic Belt in SW Mongolia: early Paleozoic rifting followed by late Paleozoic accretion. *Am. J. Sci.* 310, 523–574.
- Kröner, A., Alexeiev, D.V., Rojas-Agramonte, Y., Hegner, E., Wong, J., Xia, X., Belousova, E., Mikolajchuk, A., Seltmann, R., Liu, D., Kisilev, V., 2013. Mesoproterozoic (Grenville) terranes in the Kyrgyz north Tianshan: zircon ages and Nd–Hf isotopic constraints on the origin and evolution of basements in the southern Central Asian Orogen. *Gondwana Res.* 23, 272–295.
- Kröner, A., Kovach, V., Belousova, E., Hegner, E., Armstrong, R., Dolgoplova, A., Seltmann, R., Alexeiev, D.V., Hoffmann, J.E., Wong, J., Sun, M., Cai, K., Wang, T., Tong, Y., Wilde, S.A., Degtyarev, K.E., Rytik, E., 2014. Reassessment of continental growth during the accretionary history of the Central Asian Orogenic Belt. *Gondwana Res.* 25 (1), 103–125.
- Kuscu, G.G., Floyd, P.A., 2001. Mineral compositional and textural evidence for magma mingling in the Saraykent volcanics. *Lithos* 56, 207–230.
- Kusky, T.M., Li, J.H., 2003. Paleoproterozoic tectonic evolution of the North China craton. *J. Asian Earth Sci.* 22 (4), 383–397.
- Le Maitre, R.W.B., Dudek, P., Keller, A., Lameyre, J., Le Bas, J., Sabine, M.J., Schmid, P.A., Sorensen, R., Streckeisen, H., Woolley, A., Zanettin, A.R., 1989. *A Classification of Igneous Rocks and Glossary of Terms: Recommendations of the International Union of Geological Sciences, Subcommittee on the Systematics of Igneous Rocks (No. 552.3 CLA): International Union of Geological Sciences*. Blackwell, Oxford (193 p).
- Li, J.Y., 2006. Permian geodynamic setting of Northeast China and adjacent regions: closure of the Paleo–Asian Ocean and subduction of the Paleo–Pacific plate. *J. Asian Earth Sci.* 26, 207–224.
- Li, W.B., Zhong, R.C., Xu, C., Song, B., Qu, W.J., 2012. U–Pb and Re–Os geochronology of the Bainaimiao Cu–Mo–Au deposit, on the northern margin of the North China craton, Central Asia Orogenic Belt: implications for ore genesis and geodynamic setting. *Ore Geol. Rev.* 48, 139–150.
- Li, Y.L., Zhou, H.W., Brouwer, F.M., Xiao, W.J., Wijbrans, J.R., Zhong, Z.Q., 2014. Early Paleozoic to middle Triassic divergent accretion in the Central Asian Orogenic Belt: insights from zircon U–Pb dating of ductile shear zones in central Inner Mongolia, China. *Lithos* 205, 84–111.
- Liang, Q., Jing, H., Gregoire, D.C., 2000. Determination of trace elements in granites by inductively coupled plasma mass spectrometry. *Talanta* 51 (3), 507–513.
- Liu, J., Mao, J.W., Wu, G., Wang, F., Luo, D.F., Hu, Y.Q., 2014. Zircon U–Pb and molybdenite Re–Os dating of the Chalukou porphyry Mo deposit in the northern Great Xing'an Range, China and its geological significance. *J. Asian Earth Sci.* 79, 696–709.
- Liu, C.F., Wu, C., Zhu, Y., Zhou, Z.G., Jiang, T., Liu, W.C., Li, H.Y., 2015. Late Paleozoic–Early Mesozoic magmatic history of the central Inner Mongolia, China: implications for the tectonic evolution of the Xingmeng Orogenic Belt, southeastern segment of the Central Asian Orogenic Belt. *J. Asian Earth Sci.* <http://dx.doi.org/10.1016/j.jseaes.2015.09.011> (in press).
- Ludwig, K.R., 2003. *User's manual for Isoplot 3.00: a geochronological toolkit for Microsoft Excel*. Berkeley Geochronology Center Special Publication 4. 70 (Berkeley, USA).
- Ludwig, K.R., 2004. *Isoplot/Ex, version 3.00: A geochronological toolkit for Microsoft Excel*. Berkeley Geochronology Center, Berkeley, CA.
- Maniar, P.D., Piccoli, P.M., 1989. Tectonic discrimination of granitoids. *Geol. Soc. Am. Bull.* 101, 635–643.
- Manning, D.A.C., 1981. The effect of fluorine on liquidus phase relationships in the system Qz–Ab–Or with excess water at 1 kb. *Contrib. Mineral. Petrol.* 76, 206–215.
- Mao, J.W., Zhang, Z.H., Yu, J.J., Niu, B.G., 2003. Geodynamic settings of Mesozoic large-scale mineralization in North China and adjacent areas—implication from the highly precise dating of ore deposits. *Sci. China Ser. D Earth Sci.* 46, 838–851.
- Mao, J.W., Xie, G.Q., Zhang, Z.H., Li, X.F., Wang, Y.T., Zhang, C.Q., Li, Y.F., 2005. Mesozoic large-scale metallogenic pulses in North China and corresponding geodynamic settings. *Acta Petrol. Sin.* 21, 169–188 (in Chinese).
- Mao, J.W., Cheng, Y.B., Chen, M.H., Pirajno, F., 2013. Major types and time-space distribution of Mesozoic ore deposits in South China and their geodynamic settings. *Mineral. Deposita* 48, 267–294.
- Mao, J.W., Pirajno, F., Lehmann, B., Luo, M.C., Berzina, A., 2014. Distribution of porphyry deposits in the Eurasian continent and their corresponding tectonic settings. *J. Asian Earth Sci.* 79, 576–584.
- McCutcheon, S.R., 1990. *The Late Devonian Mount Pleasant Caldera Complex: Stratigraphy, Mineralogy, Geochemistry and Geologic Setting of a Sn–W Deposit in Southwestern New Brunswick*. Unpublished PhD thesis. Dalhousie University.
- Halifax, Nova Scotia, Canada McCutcheon, S.R., Robinson, P.T., 1988. Embayed volcanic quartz: a product of cellular growth Q rather than resorption. *Marit. Sediments Atl. Geol.* 24, 203.
- Meinert, L.D., 1992. Skarn and skarn deposit. *Geosci. Can.* 19, 145–162.
- Meinert, L.D., Dipple, G.M., Nicolescu, S., 2005. World skarn deposit. *Econ. Geol.* 100, 299–336.
- Middlemost, E.A.K., 1994. Naming materials in the magma/igneous rock system. *Earth Sci. Rev.* 37, 215–224.
- Miller, C.F., McDowell, S., Mapes, R., 2003. Hot and cold granites? Implications of zircon saturation temperatures and preservation of inheritance. *Geology* 6, 529–532.
- Nekvasil, H., 1991. Ascent of felsic magmas and formation of rapakivi. *Am. Mineral.* 76, 1279–1290.
- Nie, F.J., Zhang, W.Y., Du, A.D., Jiang, S.H., Liu, Y., 2007. Re–Os isotopic age dating of molybdenite separates from the Chaobuleng skarn iron polymetallic deposit, Dong Ujimqin Banner, Inner Mongolia. *Acta Geosci. Sin.* 28 (4), 315–323.
- Pearce, J.A., 1996. Sources and settings of granitic rocks. *Episodes* 19, 120–125.
- Pearce, J.A., Harris, N.B.W., Tindle, A.G., 1984. Trace element discrimination diagrams for the tectonic interpretation of granitic rocks. *J. Petrol.* 25, 956–983.
- Rickwood, P.C., 1989. Boundary lines within petrologic diagrams which use oxides of major and minor elements. *Lithos* 22, 247–263.
- Rollinson, H.R., 2014. *Using Geochemical Data: Evaluation, Presentation, Interpretation*. Routledge (352 p).
- Sakuyama, M., 1979. Evidence of magma mixing; petrological study of Shirouma–Oike calc-alkaline andesite volcano, Japan. *J. Volcanol. Geotherm. Res.* 5, 179–208.
- Sakuyama, M., 1981. Petrological study of the Myoko and Kurohime volcanoes, Japan; crystallization sequence and evidence for magma mixing. *J. Petrol.* 22, 553–583.
- Santosh, M., 2010. Assembling North China craton within the Columbia supercontinent: the role of double-sided subduction. *Precambrian Res.* 178 (1), 149–167.
- Santosh, M., Sajeev, K., Li, J.H., 2006. Extreme crustal metamorphism during Columbia supercontinent assembly: evidence from North China craton. *Gondwana Res.* 10 (3), 256–266.
- Santosh, M., Wilde, S.A., Li, J.H., 2007. Timing of Paleoproterozoic ultrahigh-temperature metamorphism in the North China craton: evidence from SHRIMP U–Pb zircon geochronology. *Precambrian Res.* 159 (3), 178–196.
- Selby, D., Creaser, R.A., 2004. Macroscale NTIMS and microscale LA–MC–ICP–MS Re–Os isotopic analysis of molybdenite: testing spatial restrictions for reliable Re–Os age determinations, and implications for the decoupling of Re and Os within molybdenite. *Geochim. Cosmochim. Acta* 68, 3897–3908.
- Sengör, A.M.C., Natal'in, B.A., 1996. Paleotectonics of Asia: fragments of a synthesis. In: Yin, A., Harrison, M. (Eds.), *The Tectonic Evolution of Asia*. Cambridge, Cambridge University Press, pp. 486–640.
- Sengör, A.M.C., Natal'in, B.A., Burtman, V.S., 1993. Evolution of the Altaid tectonic collage and Paleozoic crustal growth in Eurasia. *Nature* 364, 299–307.
- Shi, Y.R., Liu, D.Y., Miao, L.C., Zhang, F.Q., Zhang, W., Hou, K.J., Xu, J.Y., 2010. Devonian A-type granitic magmatism on the northern margin of the North China craton: SHRIMP U–Pb zircon dating and Hf–isotopes of the Hongshan granite at Chifeng, Inner Mongolia, China. *Gondwana Res.* 17, 632–641.
- Shinohara, H., Hedenquist, J.W., 1997. Constraints on magma degassing beneath the far southeast porphyry Cu–Au deposit, Philippines. *J. Petrol.* 38, 1741–1752.
- Shirey, S.B., Walker, R.J., 1995. Carius tube digestion for low-blank rhenium–osmium analysis. *Anal. Chem.* 67, 2136–2141.
- Smoliar, M.L., Walker, R.J., Morgan, J.W., 1996. Re–Os ages of group IIA, IIIA, IVA, and IVB iron meteorites. *Science* 271, 1099–1102.
- Stein, H.J., Scherstén, A., Hannah, J., Markey, R., 2003. Subgrain-scale decoupling of Re and ¹⁸⁷Os and assessment of laser ablation ICP–MS spot dating in molybdenite. *Geochim. Cosmochim. Acta* 67, 3673–3686.
- Stone, J.O., 2000. Air pressure and cosmogenic isotope production. *J. Geophys. Res.: Solid Earth* 105 (B10), 23753–23759.
- Sun, S.S., McDonough, W.F., 1989. Chemical and isotopic systematics of oceanic basalts: Implications for mantle composition and processes. In: Saunders, A.D., Norry, M.J. (Eds.), *Magmatism in the Ocean Basins*. Geological Society of London Special Publication Vol. 42, pp. 313–345.

- Sun, S.H., Yu, H., 1989. Interpretation of chemical composition and subdivision of magnesium-iron micas, part a basic substitution and biotite plane. *Sci. Geol. Sin.* 1, 33–48.
- Swanson, S.E., Fenn, P.M., 1986. Quartz crystallization in igneous rocks. *Am. Mineral.* 71, 331–342.
- Turner, S.P., Foden, J.D., Morrison, R.S., 1992. Derivation of some A-type magmas by fractionation of basaltic magma—an example from the Padthaway Ridge, South Australia. *Lithos* 28, 151–179.
- Vavra, G., Gebauer, D., Schmid, R., Compston, W., 1996. Multiple zircon growth and recrystallization during polyphase late Carboniferous to Triassic metamorphism in granulites of the Ivrea zone (southern alps): an ion microprobe (SHRIMP) study. *Contrib. Mineral. Petrol.* 122 (4), 337–358.
- Wang, B.R., Zhou, Z.G., Li, S.C., Liu, C.F., Zhou, Y., Feng, J.L., 2014. Geological characteristics and ore genesis of Chaobuleng Fe–Cu–Zn–Bi deposit in Inner Mongolia. *Mineral Deposits* 33 (2), 373–385.
- Watson, E.B., Harrison, T.M., 1983. Zircon saturation revisited: temperature and composition effects in a variety of crustal magma types. *Earth Planet. Sci. Lett.* 64, 295–304.
- Webster, J.D., 1990. Partition of F between H₂O and CO₂ fluids and topaz rhyolite melt. *Contrib. Mineral. Petrol.* 104, 424–438.
- Webster, J.D., Holloway, J.R., 1990. Partitioning of F and Cl between magmatic hydrothermal fluids and highly evolved granitic magmas. In: Stein, H.J., Hannah, J.L. (Eds.), *Orebearing Granite Systems; Petrogenesis and Mineralizing Processes*. Geol. Soc. Am. Spec. Paper. 246, pp. 21–34 Boulder, Colorado, USA.
- Whalen, J.B., Currie, K.L., Chappell, B.W., 1987. A-type granites: geochemical characteristics, discrimination and petrogenesis. *Contrib. Mineral. Petrol.* 95, 407–419.
- Wilde, S.A., Zhao, G., Sun, M., 2002. Development of the North China craton during the late Archean and its final amalgamation at 1.8 Ga: some speculations on its position within a global Palaeoproterozoic supercontinent. *Gondwana Res.* 5 (1), 85–94.
- Windley, B.F., Alexeev, D.V., Xiao, W., Kröner, A., Badarch, G., 2007. Tectonic models for accretion of the Central Asian Orogenic Belt. *J. Geol. Soc. Lond.* 164, 31–47.
- Wu, F.Y., Lin, J.Q., Wilde, S.A., Zhang, X.O., Yang, J.H., 2005a. Nature and significance of the Early Cretaceous giant igneous event in eastern China. *Earth Planet. Sci. Lett.* 233, 103–119.
- Wu, F.Y., Yang, J.H., Wilde, S.A., Zhang, X.O., 2005b. Geochronology, petrogenesis and tectonic implications of Jurassic granites in the Liaodong Peninsula, NE China. *Chem. Geol.* 221, 127–156.
- Wu, G., Chen, Y.C., Chen, Y.J., Zeng, Q.T., 2012. Zircon U–Pb ages of the metamorphic supracrustal rocks of the Xinghuadukou Group and granitic complexes in the Argun massif of the northern Great Hinggan Range, NE China, and their tectonic implications. *J. Asian Earth Sci.* 49, 214–233.
- Wu, C., Jiang, T., Liu, C.F., Liu, W.C., 2014. Early cretaceous A-type granites and Mo mineralization, Aershan area, eastern Inner Mongolia, northeastern China: geochemical and isotopic constraints. *Int. Geol. Rev.* 56 (11), 1357–1376.
- Wu, C., Jiang, T., Liu, W.C., Zhang, D., Zhou, Z.G., 2015. Early cretaceous adakitic granites and mineralization of the Yili porphyry Mo deposit in the Great Xing'an Range: implications for the geodynamic evolution of northeastern China. *Int. Geol. Rev.* 57 (9–10), 1152–1171.
- Wu, C., Jiang, T., Wu, C., Li, H.S., Li, Z., Liu, W.C., 2016a. Geochemistry, zircon U–Pb and molybdenite Re–Os dating of the Taolaituo porphyry Mo deposit in the Central Great Hinggan Range: implications for the geodynamic evolution of northeastern China. *Geol. J.* 51, 949–964.
- Wu, C., Liu, C.F., Zhu, Y., Zhou, Z.G., Jiang, T., Liu, W.C., Li, H.Y., Wu, C., Ye, B.Y., 2016b. Early Paleozoic magmatic history of central Inner Mongolia, China: implications for the tectonic evolution of the Southeast Central Asian Orogenic Belt. *Int. J. Earth Sci.* 105 (5), 1307–1327.
- Xiao, W.J., 2015. Tectonics of the Central Asian Orogenic Belt and its Pacific analogues. *J. Asian Earth Sci.* 113, 1–6.
- Xiao, W.J., Zhao, G.C., 2016. Tectonics and metallogeny of the orogenic collages in central and east Asia: preface. *Gondwana Res.* <http://dx.doi.org/10.1016/j.gr.2016.10.009> (In press).
- Xiao, W.J., Windley, B.F., Hao, J., Zhai, M.G., 2003. Accretion leading to collision and the Permian Solonker suture, Inner Mongolia, China: termination of the central Asian orogenic belt. *Tectonics* 22:1069. <http://dx.doi.org/10.1029/2002TC001484>.
- Xiao, W.J., Windley, B.F., Yuan, C., Sun, M., Han, C.M., Lin, S.F., Chen, H.L., Yan, Q.R., Liu, D.Y., Qin, K.Z., Li, J.L., Sun, S., 2009. Paleozoic multiple subduction–accretion processes of the southern Altai. *Am. J. Sci.* 309, 221–270.
- Xiao, W.J., Huang, B.C., Han, C.M., Sun, S., Li, J.L., 2010. A review of the western part of the Altai: a key to understanding the architecture of accretionary orogens. *Gondwana Res.* 18, 253–273.
- Xiao, W.J., Han, C.M., Liu, W., Wan, B., Zhang, J.E., Ao, S.J., Zhang, Z.Y., Song, D.F., Tian, Z.H., Luo, J., 2014. How many sutures in the southern Central Asian Orogenic Belt: insights from East Xijing–West Gansu (NW China)? *Geosci. Front.* 5, 525–536.
- Xu, B., Charvet, J., Chen, Y., Zhao, P., Shi, G.Z., 2013. Middle Paleozoic convergent orogenic belts in western Inner Mongolia (China): framework, kinematics, geochronology and implications for tectonic evolution of the Central Asian Orogenic Belt. *Gondwana Res.* 23 (4), 1342–1364.
- Zeng, Q.D., Liu, J.M., Qin, F., Zhang, Z.L., 2010. Geochronology of the Xiaodonggou porphyry Mo deposit in northern margin of North China craton. *Resour. Geol.* 60 (2), 192–202.
- Zhai, D.G., Liu, J.J., Wang, J.P., Yao, M.J., Wu, S.H., Fu, C., Liu, Z.J., Wang, S.G., Li, Y.X., 2013. Fluid evolution of the Jiawula Ag–Pb–Zn deposit, Inner Mongolia: mineralogical, fluid inclusion, and stable isotopic evidence. *Int. Geol. Rev.* 55, 204–224.
- Zhai, D.G., Liu, J.J., Zhang, H.Y., Yao, M.J., Wang, J.P., Yang, Y.Q., 2014. S–Pb isotopic geochemistry, U–Pb and Re–Os geochronology of the Huanggangliang Fe–Sn deposit, Inner Mongolia, NE China. *Ore Geol. Rev.* 59, 109–122.
- Zhang, L.C., Wu, H.Y., Wan, B., Chen, Z.G., 2009. Ages and geodynamic settings of Xilamulun Mo–Cu metallogenic belt in the northern part of the North China craton. *Gondwana Res.* 16 (2), 243–254.
- Zhang, Z.C., Hou, T., Santosh, M., Li, H.M., Li, J.W., Zhang, Z.H., Song, X.Y., Wang, M., 2014. Spatio-temporal distribution and tectonic settings of the major iron deposits in China: an overview. *Ore Geol. Rev.* 57, 247–263.
- Zhao, Y.M., 2013. Main genetic types and geological characteristics of iron-rich ore deposits in China. *Miner. Depos.* 32, 685–704 (in Chinese with English abstract).
- Zhao, Y.M., Zhang, D.Q., 1997. Metallogeny and Prospective Evaluation of Copper–Polymetallic Deposits in the Great Hinggan Range and its Adjacent Regions. Seismological Press, Beijing, pp. 1–318 (In Chinese with English abstract).
- Zhao, W.W., Zhou, M.F., 2015. In-situ LA–ICP–MS trace elemental analyses of magnetite: The Mesozoic Tengtie skarn Fe deposit in the Nanling Range, South China. *Ore Geol. Rev.* 65, 872–883.
- Zhao, Y.M., Lin, W.W., Bi, C.S., Li, D.X., 1986. Basic geological characteristics of skarn deposits of China. *Bull. Chin. Acad. Geol. Sci.* 14, 59–87.
- Zhao, Y.M., Lin, W.W., Bi, C.S., Li, D.X., Jiang, C.J., 1990. Skarn Deposit of China. Geological Publishing House, pp. 1–354.
- Zhao, G.C., Wilde, S.A., Cawood, P.A., Sun, M., 2001. Archean blocks and their boundaries in the North China craton: lithological, geochemical, structural and P–T path constraints and tectonic evolution. *Precambrian Res.* 107, 45–73.
- Zhao, Y., Zhang, S.H., Xu, G., Yang, Z.Y., Hu, J.M., 2004. The Jurassic major tectonic events of the Yanshanian intraplate deformation belt. *Geol. Bull. China* 23, 854–862 (in Chinese).
- Zhou, Z.X., 1986. The origin of intrusive mass in fengshandong, Hubei province. *Acta Petrol. Sin.* 2 (1), 59–70.
- Zhou, X.M., Sun, T., Shen, W.Z., Shu, L.S., Niu, Y.L., 2006. Petrogenesis of Mesozoic granitoids and volcanic rocks in South China: a response to tectonic evolution. *Episodes* 29 (1), 26–33.
- Zhou, Z.G., Zhang, T., Wang, B.R., Yu, Y.S., 2010. Disappearance of Sea Floor of the Paleo-Asian Ocean: Geological Evidence from the Dong Ujimqin, Inner Mongolia, China (AGU Fall Meeting Abstracts).
- Zhou, Z.H., Mao, J.W., Lyckberg, P., 2012. Geochronology and isotopic geochemistry of the A-type granites from the Huanggang Sn–Fe deposit, southern Great Hinggan Range, NE China: implication for their origin and tectonic setting. *J. Asian Earth Sci.* 49, 272–286.